Key Points:
- Glider observations are assimilated with and without surface observations in the challenging Columbia River plume region using 4DVAR
- Assimilation of glider observations alone can create erroneous eddy variability that will deteriorate forecast performance
- Assimilating glider in combination with surface observations suppresses these features and improves impact of glider assimilation

Why Gliders Appreciate Good Company: Glider Assimilation in the Oregon-Washington Coastal Ocean 4DVAR System With and Without Surface Observations

I. Pasmans[1] [ID] , **A. L. Kurapov[1,2]** [ID] , **J. A. Barth[1,3]**, **A. Ignatov[4]** [ID] , **P. M. Kosro[1]** [ID] , and **R. K. Shearman[1]**

[1]College of Earth, Ocean, and Atmospheric Sciences, Oregon State University, Corvallis, OR, USA, [2]NOAA Coast Survey Development Laboratory, Silver Spring, MD, USA, [3]Marine Studies Initiative, Oregon State University, Corvallis, OR, USA, [4]NOAA STAR, College Park, MD, USA

Abstract Gliders are low-power autonomous underwater vehicles used to obtain oceanic measurements in vertical sections. Assimilation of glider temperature and salinity into coastal ocean circulation models holds the potential to improve the ocean subsurface structure estimate. In this study, the impact of assimilation of glider observations is studied using a four-dimensional variational (4DVAR) data assimilation and forecast system set offshore of Oregon and Washington on the U.S. West Coast. Four test cases are compared: (1) no assimilation, (2) assimilation of glider temperature and salinity data alone, (3) assimilation of the glider data in combination with the surface observations including satellite sea surface temperature, sea surface height, and high-frequency radar surface velocities, and (4) assimilation of the surface data alone. It is found that the assimilation of glider observations alone creates unphysical eddies in the vicinity of the glider transect. As a consequence, the forecast errors in the surface velocity and temperature increase compared to the case without data assimilation. Assimilation of surface and subsurface observations in combination prevents these features from forming and reduces the errors in the forecasts for the subsurface fields compared to the other three experiments. These improvements persisted in 21-day forecasts run after the last data assimilation cycle.

Plain Language Summary Ocean forecast systems, like our system for the ocean offshore Oregon-Washington, USA, use numerical models to predict future temperature, currents, sea surface height, and salt concentration. Eventually, these predictions are corrected using observations in a process called data assimilation (DA) in order to better approximate the true state of the ocean. Assimilation of subsurface observations made by autonomous underwater vehicles called gliders can potentially improve the predictions of the ocean state below the surface. In this study, we have assimilated glider observations together with, and in absence of, surface observations. We found that assimilation of glider observations alone creates predictions that are less accurate than those obtained from a model without DA as the DA creates unphysical features. Assimilating the glider observations in tandem with surface observations prevents these features from forming and realizes local improvements to the subsurface ocean predictions that last for 21 days after the last DA correction. These results show that one has to be careful with using glider observations in DA and should always assimilate glider observations in combination with observations that cover large swaths of the ocean surface.

1. Introduction

The Oregon State University (OSU) coastal ocean forecast system provides daily updates of 3-day forecasts of shelf currents, temperature, and other physical variables of interest along the Oregon (OR) and Washington (WA) coasts (Erofeeva, 2018; NANOOS, 2018). The information provided by the system has been used as guidance by local fishermen, a government agency in charge of environmental hazard response, and other users. The system uses data assimilation (DA) to improve the accuracy of initial conditions for the forecasts. Currently, only surface observations are assimilated, including satellite sea surface temperature

(SST), satellite sea surface height (SSH; Kurapov et al., 2011), and surface currents from a network of land-based high-frequency radars (HFR; Yu et al., 2012). No subsurface in situ observations are included as their availability has been limited. The ongoing Ocean Observatories Initiative (2018) project includes an effort for regular deployment of a fleet of gliders, autonomous platforms capable of making subsurface in situ measurements, along several lines in this region. The possibility of using these measurements in our forecast system has encouraged us to investigate the impact of glider DA using the 2011 archive data from just one glider section in Oregon.

The subsurface salinity (S) and temperature (T) measurements taken by the gliders can potentially provide a valuable constraint on the subsurface stratification and location of fronts and eddies along the glider path. However, assimilation in short time intervals will use data only along a limited segment of the track and will most probably result in local corrections to the vertical stratification, in particular, if a relatively short (25–50 km) horizontal decorrelation scale is assumed for the model background errors (Kurapov et al., 2011). If the background error covariance implies dynamical balances in the correction, including geostrophy and thermal wind balance (Weaver et al., 2005), this local correction in the vertical stratification will yield horizontal density gradients that will be balanced by a correction in the baroclinic currents. These corrections will take the form of eddies that could potentially degrade the forecasts. Even if the balanced covariance is not utilized, the local correction in initial conditions for the density will eventually be balanced by changes in the velocity field by dynamical adjustment. So we hypothesize that in situ hydrographic profile data assimilation can result in spurious baroclinic eddy generation that will deteriorate forecasts. Since surface observations including satellite SST, SSH, and HFR surface currents all contain information about the eddies, their assimilation in combination with the in situ glider data can potentially allow the fit to the subsurface data without erroneous eddy generation. In that case the correction to the vertical stratification can potentially extend to distances larger than the Rossby radius of deformation.

Reports of earlier test studies involving glider DA are a mixture of success stories and signs of complications. Pan et al. (2014) compared results of glider DA to mooring data west of Florida and found a reduction of the root-mean-square error (RMSE) with respect to mooring T and S in the forecasts compared to the control run (model without DA). Jones et al. (2012) compared the DA analyses and the no-DA model results southeast of Tasmania and found reduction in the nearshore mooring temperature RMSE as well as a 40% reduction in the RMSE in satellite SST observations that were not assimilated. Shulman et al. (2009) found that after assimilating data from 10–15 gliders in an approximately 100 × 200-km area near Monterey Bay (Central California), the RMSE in mooring temperature and salinity decreased and the correlation between mooring temperature, salinity, and velocities increased compared to a model without DA. These studies do not report on adverse eddy variability introduced by the glider assimilation. In both Shulman et al. (2009) and Jones et al. (2012), the data assimilation correction was added to the model in small increments to avoid shocks to the system. This potentially helped to alleviate the problem of bogus eddy variability. Ngodock and Carrier (2014) assimilated several glider transects in Monterey Bay in combination with SST and SSH and found a lower number of large discrepancies between observations and forecast predictions than in the control run. Zhang et al. (2010) assimilated glider observations in combination with HFR currents and satellite SST in the New York Bight. They reported 25–60% reduction in the analysis RMSE for these observations (i.e., data fits) compared to forecasts. Reduction of the subsurface temperature was attributed in part to SST assimilation. Matthews et al. (2012) assimilated SST, SSH, and subsurface glider T and S and also found reductions in the RMSE for these observations in the analyses (up to 40%) compared to a control (no-DA) run. At the same time, Melet et al. (2012) disclose that assimilation of T and S from 10 gliders off Samoa actually produced analyses with higher RMSEs in the model T and S fields than in the control run serving as truth. Li et al. (2013) found that assimilation of glider observations alone created spurious small-scale structures in the surface velocity field in Prince William Sound, Alaska. Dobricic et al. (2010) found that assimilation of glider observations alone in the eastern Ionic Sea reduced the RMSE in the surface and subsurface temperature and salinity observations but increased RMSEs in SSH and current observations in the top 200 m of the water column by as much as 23% compared to the control run.

In this study, we want to find ways in which glider observations can be assimilated usefully in our OR-WA coastal ocean forecast system. In particular, we will test the following hypotheses: (1) assimilation of glider observations alone in an area of the continental shelf and slope can create unobserved eddy variability and degrade the forecast accuracy; (2) assimilation of the glider observations in combination with surface observations yields better forecast error statistics than those obtained by assimilating only glider observations

or only surface observations; (3) combined surface glider data assimilation can help extend the zone of impact of the glider data beyond the direct vicinity of the glider transect. This study looks at a combination of conditions that have not been considered in previous studies: it uses a four-dimensional variational (4DVAR) DA system in a series of time intervals, the glider is assimilated along only one transect and is located in the immediate vicinity of a seasonal upwelling front with a large river plume being present on the offshore side of the upwelling front. Furthermore, we make a comparison of the non-DA model, the glider-only, combined glider-surface and surface-only DA cases and focus not only on the data fits (analyses) but also on 3-day and longer-term forecasts.

This article is arranged as follows: Section 2 describes the model setup, the assimilated observations, and our DA system. Section 3 looks at the corrections in these experiments and the accuracy of the forecasts in the different cases. Finally, section 4 will conclude to what extent the results agree or disagree with our three hypotheses.

2. The Dynamical Regime and the Model Setup

2.1. Dynamical Regime
The model domain is shown in Figure 1. The summer conditions in this region are characterized by predominantly southward winds that force offshore Ekman transport in the surface layer, upwelling, and a baroclinic equatorward coastal jet (Huyer, 1977, 1983; Kosro, 2005; Mooers et al., 1976). As the upwelling develops, the coastal current exhibits instabilities and jets separate off the shelf carrying cold, nutrient-rich coastal waters offshore (Barth et al., 2000; Koch et al., 2010; Oke, Allen, Miller, Egbert, Austin, et al., 2002; Oke, Allen, Miller, Egbert, & Kosro, 2002, Oke, Allen, Miller, & Egbert, 2002). The near-surface salinity variability in our study domain is influenced by the outflow of the Columbia River at 46.25°N (Hickey et al., 1998). Here we use the 31.5 isohaline contour from our model solution to show the edge of the plume. During winter the river plume flows northward along the Washington coast. During summer the wind and coastal upwelling displace the plume south and offshore (dashed line in Figure 1). During periods of relaxation from upwelling conditions and episodic downwelling events, the plume is pressed against the Oregon coast south of the river mouth (solid line) (Hickey et al., 2005; Liu et al., 2009).

2.2. Model
The ocean state is simulated using the Region Ocean Modeling System (ROMS) version 3.6 (www.myroms.org). This is a nonlinear, finite volume, hydrostatic, Boussinesq model featuring advanced numerics (Shchepetkin & McWilliams, 2003, 2005). The model grid resolution is approximately 2×2 km in the horizontal and 40 terrain-following layers in the vertical direction. Baroclinic modes are resolved using a time step of 90 s, while the barotropic time step is 3 s. The bathymetry is obtained by averaging depths from the U.S. Coastal Relief Model (National Centers for Environmental Prediction, NCEP, 2015a) and ETOPO2 (NCEP, 2015b) and smoothed as in Sikirić et al. (2009). Boundary forcing is taken from the Hycom-NCODA 1/12° analysis (COAPS, 2015), while barotropic tidal components at the boundary are added from the TPXO tidal model (Egbert & Erofeeva, 2002, 2013). The boundary conditions are imposed using Chapman (1985) for the free surface, Flather (1976) for the barotropic velocities, and mixed radiation-nudging for the baroclinic velocities, temperature, and salinity (Marchesiello et al., 2001). Surface momentum and heat fluxes are calculated using the ROMS bulk flux parameterization. The wind, surface air pressure, net short-wave radiation, downward long-wave radiation, air temperature, and relative humidity fields required by the bulk flux parameterization (Fairall et al., 2003) are taken from the North American Mesoscale analysis (NCEP, 2015c). The model does not include evaporation or precipitation. Mellor-Yamada 2.5 is used as the turbulent closure scheme (Mellor & Yamada, 1982). The Columbia River estuary is represented as an idealized 50-km-long channel. The Columbia River together with 15 rivers in the Salish Sea (Banas et al., 2015) are implemented as point sources with a uniform discharge throughout the water column. The Columbia River discharge is based on measurements at the U.S. Geological Survey Beaver Army Terminal (USGS, 2015). The river temperature is provided as climatology based on several years of observations at the same station. The discharge and river temperature of the Fraser River and the small rivers in Puget Sound are based on the climatology obtained from data measured by Environment Canada (2015); USGS (2015) and provided by P. MacCready and S. Giddings (Giddings et al., 2014; MacCready & Giddings, 2016). During the analysis period (21 July to 11 August) the river discharge of the Columbia River varies between 6.3 and 9.6×10^3 m^3/s with a mean of 7.7×10^3 m^3/s, which is anomalously high compared to the average discharge of 6.0×10^3 m^3/s
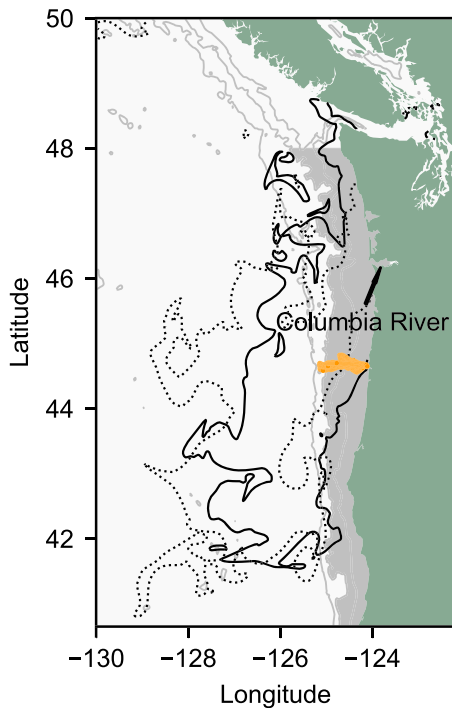
Figure 1. Overview of the model region together with the assimilated glider transects (orange), the 200, 1,000, and 2,000-m isobaths (gray lines) and the coastal shelf region used in the surface observation comparison in Figures 14 and 15 (gray). Also shown are the 31.5 isohaline on 21 July 2011 (black solid line) and the extent of the Columbia River plume on 13 August 2011 (dotted black line) according to the model without DA.

(USGS, 2015). The cumulative outflow of the other rivers varies between 3.8 and 5.3 × 10³ m³/s with a mean of 4.6 × 10³ m³/s. Model runs were carried out on a local cluster at OSU as well as the COMET supercluster via the XSEDE framework (Towns et al., 2014).

2.3. Surface Observations

Along the Oregon coast, a network of seven HFR stations was in place in 2011 primarily covering the Oregon shelf and shelf break between 41°N and 46°N. Hourly radial surface velocity components are available from each site (Kosro, 2017). Observations are binned into superobservations by vector averaging in approximately 5 × 5-km boxes. If the directional spread of the velocities within a box is more than 9°, the observations in the box are rejected. Hourly time series in a single day are verified at each point and incomplete series are also rejected. The full time series at a point is averaged over a day, and the daily averaged data are matched to the daily averaged model radial component estimate at the same point.

SST is obtained from NOAA19 and Metopa-A satellites (Ignatov et al., 2016). For each hour the observations, which are available on a 0.02° × 0.02° grid, are binned into the cells of a 4 × 4-km grid, and the observations within each grid cell are averaged to create super observations. Starting from the end of a 3-day data assimilation window and working toward the beginning, the resulting observations are then thinned such that the time between two observations in the same grid cell is at least 3 hr. These observations are assimilated as instantaneous point measurements.

Alongtrack sea surface anomaly plus the mean dynamic topography from the Jason-1, Jason-2, Cryosat, and Envisat satellites are obtained from Scharroo et al. (2013). The slope in these observations provides information about relatively slowly changing, subinertial, surface geostrophic currents, and these data are used to constrain the nontidal, 24-hr averaged model SSH slope. To match these data and the tide-resolving model, the following procedure is used. Model tidal harmonic constants are obtained from the analysis of a long no-DA run with T_TIDE (Pawlowicz et al., 2002). The model tidal SSH is computed using eight dominant harmonic constants at the points along the altimetry track for a 24-hr period centered around the observation time. This signal is then time averaged and added to the satellite-derived absolute dynamic topography. Geographically correlated errors are known to contribute significantly to the total altimetry error (Dettmering & Bosch, 2010; Labroue et al., 2012). To remove these large-scale errors as much as possible, the mean of each track through the model domain is calculated and removed. In the DA scheme, the resulting observation is matched to the 24-hr-averaged model SSH minus the along-track mean.

2.4. Subsurface Observations

Glider temperature and salinity observations along the Newport line (44.65°N, see Figure 1) are available on a grid with a 1-km resolution in the horizontal direction, along the glider track, and 4 m in the vertical direction. The profiles are provided together with the variance of the raw observations for each point (Erofeev, 2015; Mazzini et al., 2014; Saldías et al., 2016). For each vertical profile the observations are boxed and averaged within each model grid cell. Observational variances for the boxed glider observations are calculated as follows:

$$\sigma_\xi^2 = \frac{1}{M}\sum_{j=1}^{M}\sigma_{\xi,j}^2 + \frac{1}{M}\sum_{j=1}^{M}(\xi_j - \overline{\xi})^2, \tag{1}$$

where ξ is either glider T or S, M is the number of profile observations in the box, $\sigma_{\xi,j}$ is the standard deviation of the jth observation as specified in the data, and $\overline{\xi}$ is the average of the observations in the box. An additional $(5.7 \cdot 10^{-2}\,°C)^2$ or $(1.30 \times 10^{-2})^2$ is added to this to account for the measurement error variance in T or S, correspondingly. These boxed and averaged observations are assimilated as instantaneous point measurements.

2.5. Data Assimilation

DA proceeds in a series of 3-day windows. In each window, the correction to the initial conditions is found using the Advanced Variational Regional Ocean Representer Analyzer (AVRORA) 4DVAR system developed in-house (Kurapov et al., 2009, 2011; Yu et al., 2012). The AVRORA tangent linear and adjoint codes are algorithmically and dynamically consistent with the nonlinear ROMS, and their modular structure is very suitable to experimentation with different background error covariances (Pasmans & Kurapov, 2017) and data functionals. In particular, we can easily implement assimilation of the SSH slope (see Kurapov et al. 2011) or daily averaged observations.

After the corrected initial conditions are obtained using AVRORA 4DVAR, the nonlinear ROMS is run for the 3 days, to yield the analysis, and is continued for another 3 days providing the forecast. The forecast, saved hourly, provides the background solution for linearization in the next assimilation window. The correction $\delta\vec{x}$ to the ocean state at the beginning of the forecast is found by minimizing the penalty function (Courtier et al., 1994):

$$J(\delta\vec{x}) = \frac{1}{2}\delta\vec{x}^T \mathbf{B}^{-1} \delta\vec{x} + \frac{1}{2}(\vec{d} - \mathbf{HM}\delta\vec{x})^T \mathbf{R}^{-1}(\vec{d} - \mathbf{HM}\delta\vec{x}). \qquad (2)$$

Here $\mathbf{M}$ is the tangent linear model, that is, the nonlinear model linearized around the forecast on a 4×4-km grid, $\mathbf{H}$ is the linear operator that maps the ocean state to the space of observations, $\vec{d}$ is the innovation vector, that is, the difference between the observations and the predictions for those observations obtained by applying $\mathbf{H}$ to the forecast, $\mathbf{R}$ is the observation error covariance, and $\mathbf{B}$ is the background error covariance, that is, the covariance of the errors present in the ocean state at the beginning of the forecast. ^{T} denotes the matrix transpose.

As $\mathbf{B}$, the balanced operator covariance (Weaver et al., 2005) is used with a modification to account for the shallow shelf depth (see; Kurapov et al., 2011). This covariance assumes that errors in all fields are related to background temperature errors via a simple linear temperature-salinity relation, the linear equation of state, and thermal wind balance. To speed up computations, the background temperature error covariance is assumed to be Gaussian and separable into two horizontal directions and along the vertical s coordinate. The horizontal correlation length scale in each direction is 25 km, corresponding to the open ocean Rossby radius of the deformation for the first baroclinic mode (Chelton et al., 1998). The vertical correlation scale is the same at each vertical profile in the terrain following s coordinates and is thus proportional to the total depth; it is chosen to be 15 m in 250-m-deep water. The temperature error standard deviation σ_T is reduced exponentially with depth, with the decrement $l_z = 100$ m. To estimate $\sigma_T(z)$ at the surface ($z = 0$), the daily averaged temperatures from the long free run are compared with time series data from National Data Buoy Center buoys 46015, 46022, 46027, 46029, 46041, 46050, 46087, 46088, 46089, 46094, 46211, 46229, 46243, 46244, and 46248 (NDBC, 2016) and the standard deviation of the difference is calculated for each buoy. The median of these standard deviations yields $\sigma_T(0) = 0.9\,°\mathrm{C}$.

The observational error covariance matrix $\mathbf{R}$ is assumed to be diagonal. The initial estimates of the variances for the surface observations are obtained using equations similar to (1). The observations are then rescaled based on the following expression (Bennett, 1992; Desroziers et al., 2005):

$$\mathbf{HMBM}^T\mathbf{H}^T + \mathbf{R} = \langle \vec{d}\vec{d}^T \rangle \qquad (3)$$

where $\langle \cdot \rangle$ is the statistical average. Here we approximate the statistical average by the spatial average. Or more specifically, for the window 9–11 July we estimate the background surface error variance using different types of observations in the top 6 m of the water column by $\langle d_i^2 - \mathbf{R}_{ii} \rangle_\xi$, where ξ denotes the observation type, i runs over the observations of this type, and $\mathbf{R}_{ii} = \sigma_\xi^2$ is the initial estimate of the error variance of the ith observation. Based on this comparison we find that the background error standard deviation for surface temperature should be rescaled by a factor $\alpha_{\mathrm{glider},T} = 1.3$ (glider) or $\alpha_{\mathrm{SST}} = 1.1$ (satellite). Similarly, surface salinity should be rescaled by $\alpha_{\mathrm{glider},S} = 12.5$, surface height by $\alpha_{\mathrm{SSH}} = 8.4$ (SSH) and surface velocities by $\alpha_{\mathrm{HFR}} = 3.8$ (HFR). The balanced operator does not allow to change the background error variance for different fields separately by multiplying each of them with α_ξ^2. Instead, we multiply the diagonal elements of $\mathbf{R}$ with α_ξ^{-2} for all observations of type ξ. For the surface observations we eventually fix $\sigma_{\mathrm{SST}} = 0.39\,°\mathrm{C}$, $\sigma_{\mathrm{HFR}} = 4.86\,\mathrm{cm/s}$, $\sigma_{\mathrm{SSH}} = 6.9$ mm. As the glider observational error variance varies strongly with depth, $\sigma_{\mathrm{glider},T}$ and $\sigma_{\mathrm{glider},S}$ are not adjusted using the same technique. Instead, they are found by applying the scaling to observational error variances found using (1). To prevent overfitting the glider
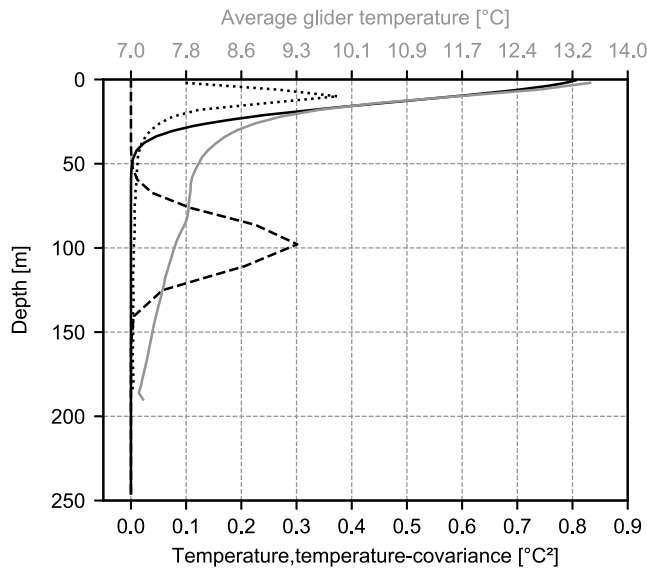
Figure 2. Background error temperature-temperature covariance between a point on the surface at 124.843°W,43.005°N and the vertical (solid black), covariance between a point at 100-m depth and the vertical (dashed black) and the time-averaged observational variance (i.e., part of the diagonal of **R**) for the glider temperature observations as used in the 4DVAR algorithm (dotted black). Also shown is the time-averaged vertical temperature profile obtained from glider observations over the period 21 July to 14 August 2011 (solid gray).

data, we limit $\sigma_\xi(z) \geq \hat{\sigma}_\xi \exp(z/l_z)$ where ξ is either glider temperature or salinity and $\hat{\sigma}_\xi$ is the median of the rescaled observational error standard deviation in the top 6 m. As Figure 2 shows, the resulting values of σ_T^2 decay rapidly with depth. The impact of outliers is reduced by rescaling $\mathbf{R}_{ii}$ to $(0.1|\vec{d}_i|)^2$ if $|\vec{d}_i| > 10\sqrt{\mathbf{R}_{ii}}$.

Minimization of (2) is carried out using the Restricted B-preconditioned Conjugate Gradient method (RBCG) (Gürol et al., 2014). Out of time considerations, minimization of (2) is terminated after 14 inner loop iterations. Also, out of time considerations, no outer loop iterations are performed. Limited parallelization is implemented by using the Orthogonal Multiple Search Direction Conjugate Gradient method (MSDO-CG; Grigori et al., 2016). In this method four new search directions are generated per iteration eventually creating a correction that lies in a subspace of dimension 56. In this respect the current AVRORA implementation differs from the one in Kurapov et al. (2009, 2011) and Yu et al. (2012).

2.6. Experiments

The model was started on 2 January 2011 from the global Navy Hycom analysis results. After making local corrections to the bathymetry to compensate for insufficient tidal mixing and thus reducing the model SST warm bias in the Strait of Juan the Fuca, the model was restarted from 27 February 2011 and ran till 1 October 2011. This case is referred to as the long free model run. To make sure glider DA results are not overshadowed by the shock of DA initialization, we first spin up DA starting on 7 July assimilating SSH, SST, and HFR velocities (see the experiment time line in Figure 3). The output of this DA model (case *Surface Only*) on 21 July is then used as the initial condition for comparing this case and the other three base test cases. In the case *No DA*, data are not assimilated after 21 July. In the *Glider Only* DA case, glider T and S are only assimilated. In the *Combined* DA case, all aforementioned observations are used. The last DA correction (cases Surface Only, Glider Only, and Combined) takes place on 8 August 2011. After this, all the experiments are continued as forecasts without further assimilation until 1 September 2011. In spring 2011 the freshwater transport from the Columbia River was anomalously large, creating a large river plume. Upwelling favorable winds preceding the DA period (see Figure 4a) turned the plume toward Oregon and offshore (Hickey et al., 2005; Liu et al., 2009). Additional upwelling events take place
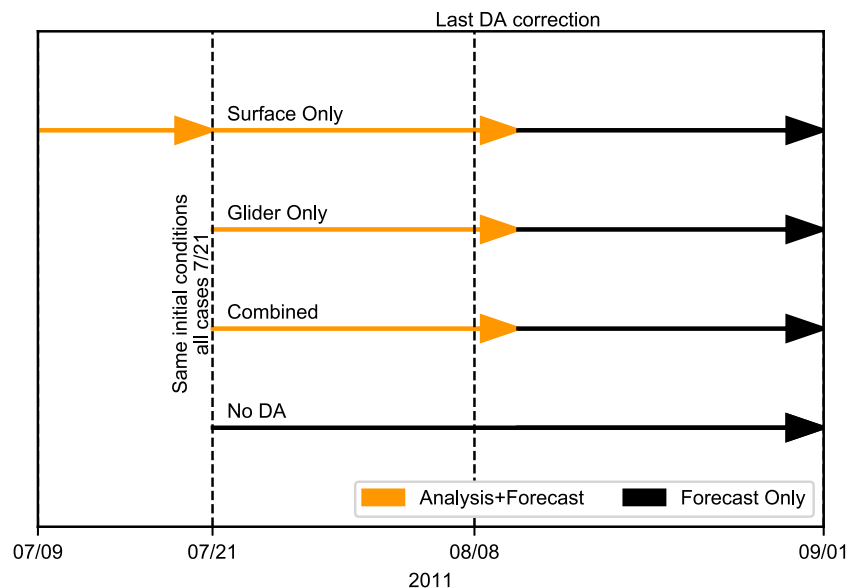

Figure 3. The experiment time line.
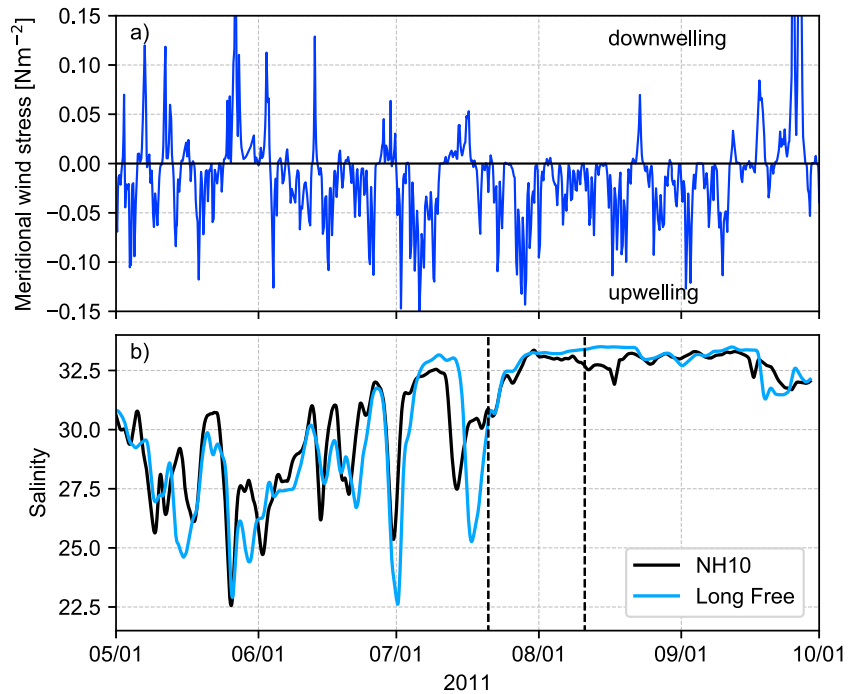
Figure 4. (a) Meridional wind stress applied to the models close to the glider transects at 124.308°W, 44.634°N. The negative wind stress corresponds to upwelling favorable northerly winds. (b) The surface salinity measured at 2-m depth at the NH10 buoy (124.308°W, 44.634°N) (black) and obtained from the long free model run without DA (blue) both filtered using a double application of a 24-h running mean filter. The assimilation period (21 July to 11 August) is marked by the vertical dashed lines.
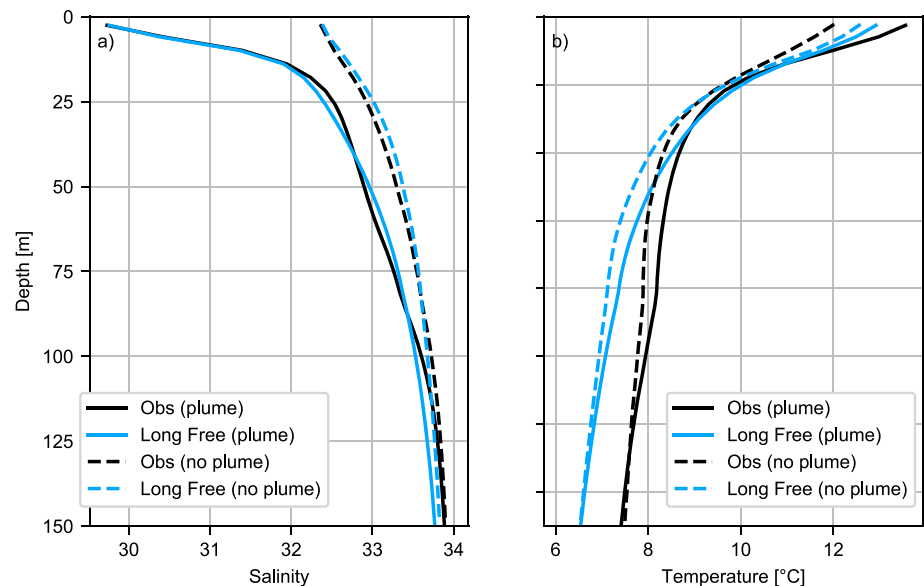
Figure 5. Time-averaged vertical profiles of (a) salinity and (b) temperature between 1 May and 1 October 2011 based on (black) glider observations and (blue) the long free model run. Solid (dashed) lines are the averages of the profiles when the Columbia River plume was present (absent) in the observations, that is, when surface $S < 31.5$ (>31.5).
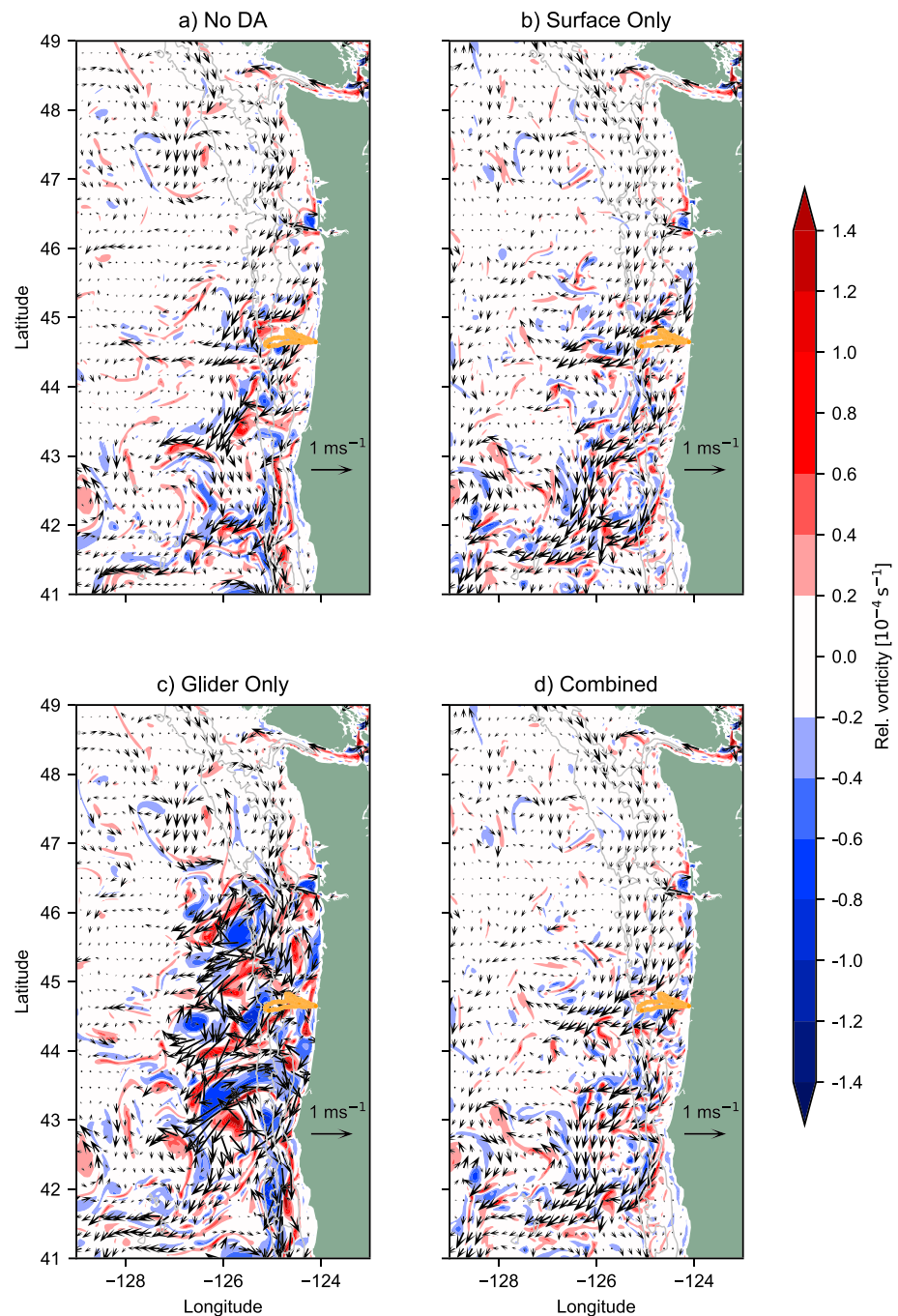
Figure 6. Daily averaged surface velocity fields (arrows) and relative vorticity in the top model layer (color scale) on 4 August 2011 from (a) the experiment without data assimilation, (b) analysis from Surface Only, (c) analysis from Glider Only, and (d) analysis from Combined. The location of the glider measurements up to 4 August 2011 24:00 is indicated by the orange lines. Gray lines mark the 200-, 1,000-, and 2,000-m isobaths.

during the DA period between 21 and 30 July and between 6–8, 11–14, and 16–22 August (see Figure 4a). The assimilation experiments are set purposely during this period, when the salinity signal sampled by the glider is particularly strong.

The model without assimilation reproduces the plume dynamics qualitatively correctly. For instance, the extent and geometry of the plume is similar to that revealed in satellite ocean color data (Saldías et al., 2016). Events of surface water freshening over the Oregon shelf following upwelling wind relaxation and
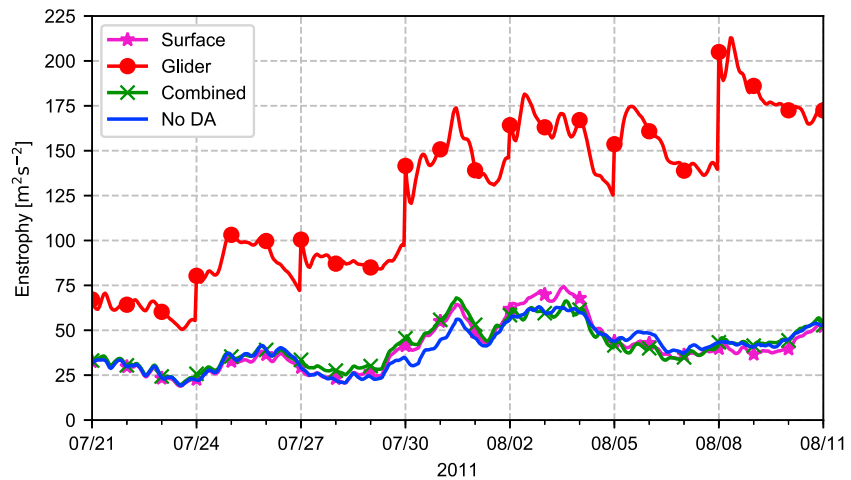
Figure 7. Enstrophy for the area between 42°N, 47°N, 127°W and the coast for the case No DA (blue) and the analysis from the cases Glider Only (red), Surface Only (purple), and Combined (green). The vertical grid lines mark the beginning of each DA window, when instantaneous correction is applied. DA = data assimilation.

reversal are observed at the NH10/NDBC46094 mooring (124.308°W, 44.634°N, see NDBC 2016). The timing and magnitude of these events is predicted well by the long free model without DA (Figure 4b). A further comparison is provided in Figure 5. This figure shows the average T and S profiles from glider observations and from the long free run without DA for the period 1 May 2011 to 1 October 2011. Different profiles are compiled for times during which the plume was present at the surface (glider surface salinity < 31.5) and during times it was not. In general, the model, even without DA, is able to reproduce the time-averaged temperature and salinity profiles in the top 150 m along the glider transect. On smaller time and space scales, that is, the scales we are hoping to correct with DA, incorrect prediction of the location of the plume front by the model might still lead to significant errors in the glider salinity observations.

3. Results

In this section we first demonstrate that assimilation of glider observations alone using our DA system creates erroneous eddies and that DA case Combined prevents these eddies from forming while still fitting the glider data. Then we compare forecasts from the different experiments. Additional sensitivity tests are performed by assimilating subsets of the surface data to learn which surface data types contribute most to the improved performance. Finally, the subsurface differences between the DA cases Surface Only and Combined will be compared to determine if glider assimilation impacts the topology of subsurface isopycnal layers on a regional scale.

3.1. DA Impact on Surface Fields

The negative impact of glider only DA on the geostrophic eddy field can be seen in plots of the surface relative vorticity, which is calculated by taking the curl of the daily averaged horizontal velocities in the top model layer. In Figure 6, it is shown together with the surface daily averaged currents on 4 August 2011 for the four experiments. Cases No DA, Surface Only, and Combined show similar structures except that in the DA cases separation at Cape Blanco (43°N) is qualitatively more vigorous and farther toward the west than in the case No DA. Assimilation of glider observations alone (Figure 6c) in the four time windows preceding this analysis resulted in generation of a strong eddy field that surrounds the glider transect and which is absent in the other three cases. The eddies are persistent: after creation at the beginning of the window they move and deform under influence of the current, but they remain present during the forecast and can be tracked in the future assimilation windows.

Are the large erroneous eddies implied mostly by the correction in the initial conditions, or can they result from the growth of baroclinic instabilities of the coastal jet, caused by the (relatively small) initial DA perturbation? To answer this question, we use hourly DA analysis outputs and calculate enstrophy $\frac{1}{2} \int |\nabla \times \vec{u}_s|^2 \, dA$ for the area most impacted by the eddies, between 42°N, 47°N, 127°W and the coast; here $\vec{u}_s$ is the
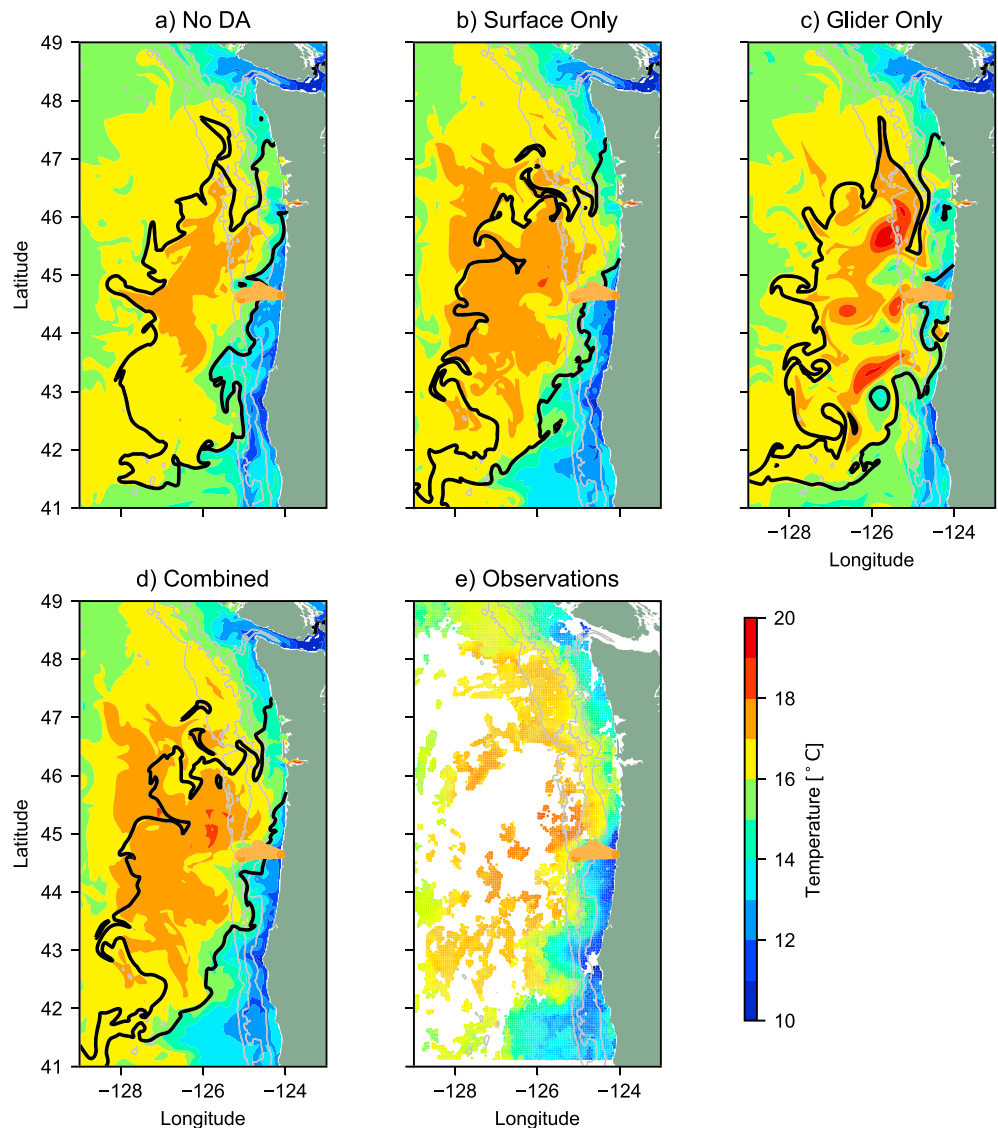
Figure 8. Daily averaged surface temperature (color scale) and the 31.5 (solid line) salinity contour on 4 August 2011 from (a) case No DA, (b) analysis from Surface Only, (c) analysis from Glider Only, (d) analysis from Combined, and (e) from satellite observations. The location of the glider measurements up to 4 August 2011 24:00 is indicated by the orange lines. Gray lines mark the 200-, 1,000-, and 2,000-m isobaths. DA = data assimilation.

horizontal surface velocity (Figure 7). We find that in the three cases, No DA, Surface Only, and Combined, the area-integrated enstrophy is remarkably similar. In case Glider Only, eddies emerging from DA increase the enstrophy by a factor of 3. The largest changes are associated with instantaneous DA corrections at the beginning of each DA window (vertical dashed lines in Figure 7). These changes are generally followed by a slow decrease of enstrophy toward the end of the 3-day window. We conclude that the enstrophy growth in the Glider Only case is mostly due to the instantaneous DA correction in the density field.

Figure 8 shows the daily averaged SST obtained from the different cases (all analysis) and satellite SST observations available on 4 August 2011, the same day as in Figure 6. The results for experiment Surface Only and Combined are nearly identical. Once again Glider Only differs significantly. Eddies are clearly visible within the Columbia River plume (solid black contours), some with a high-temperature core (>18 °C). While in the cases Surface Only and Combined the upwelling zone is continuous between 45°N and the southern boundary and is widening toward the south (in agreement with the assimilated SST), in the case Glider Only the upwelling separation zone is split into two, one over the mid-Oregon shelf and another south of Cape
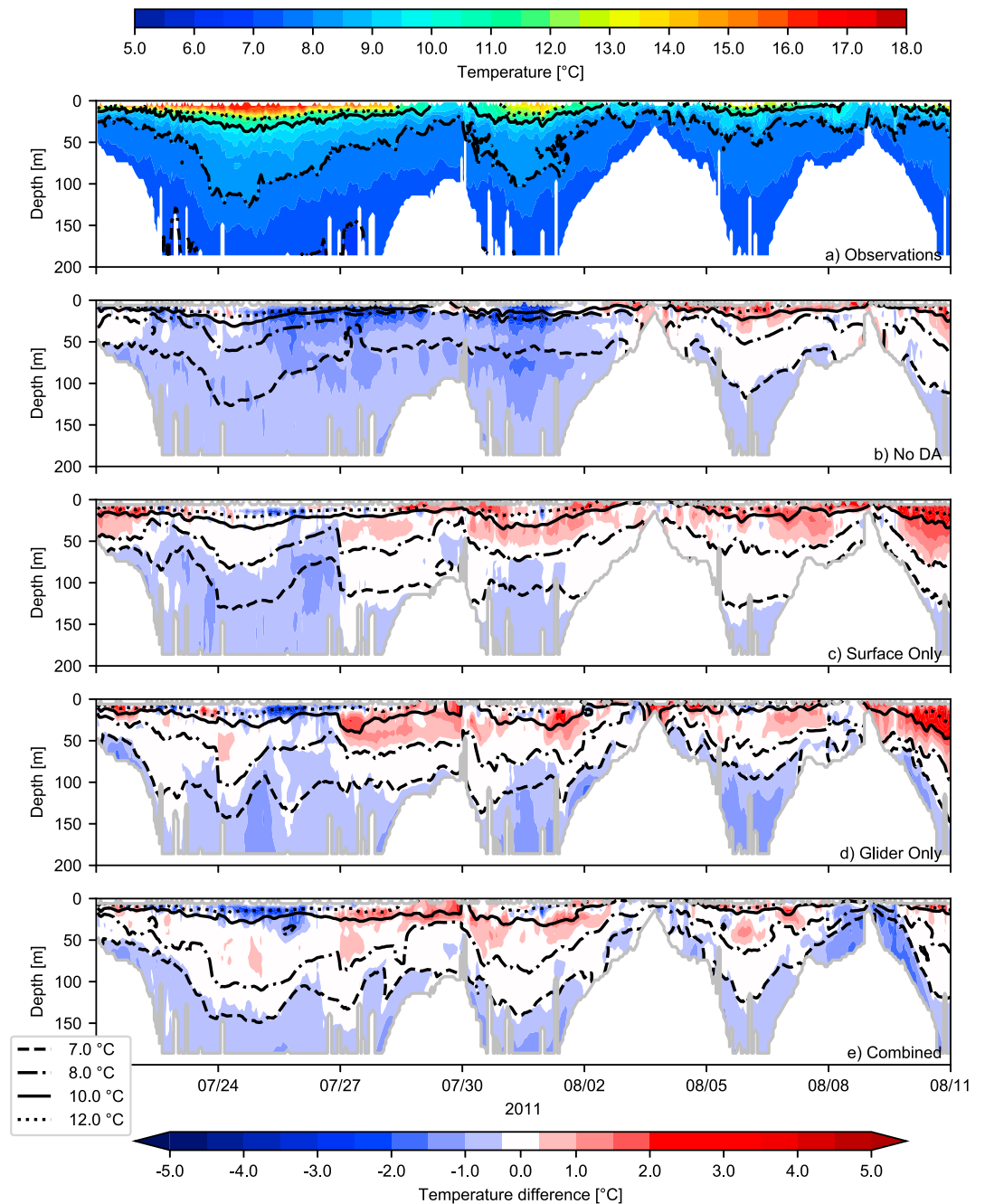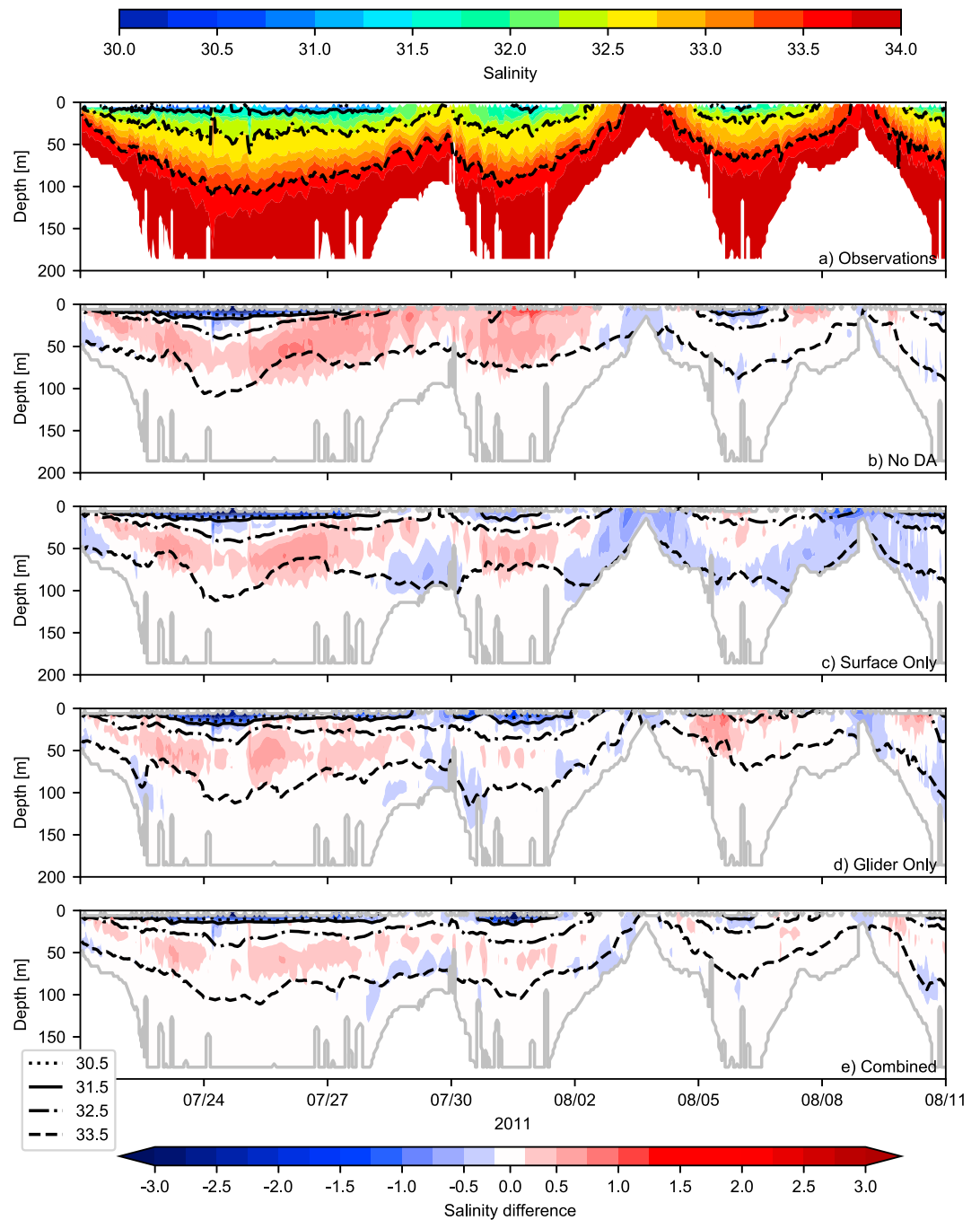
Figure 9. (a) Observed glider T as a function of time and depth; (b)–(e) the model-observation T difference, shown as color and selected model T contours, for cases (top to bottom) No DA, Surface, Glider Only, and Combined. DA analyses are used. Contours are $T = 7, 8, 10, 12\,°\mathrm{C}$.

Blanco (43°N). The eddies introduced by glider DA are not only unphysical, judged by their high enstrophy, but also damaging to the prediction of the front geometry and associated alongshore transport.

3.2. DA Impact on Subsurface Fields

Figure 9a shows glider temperature sections as a function of time and the vertical coordinate, for the period 21 July through 11 August. Below it, in Figures 9b–9e, the difference between the four base model cases and the glider temperature is shown as color. Selected temperature contours for each model case are also shown. For the DA cases (Figures 9c–9e), analysis fields are sampled along the glider path. Figure 10 exhibits similar plots for salinity and model-data salinity differences.

Figure 10. (a) Observed glider S as a function of time and depth; (b)–(e) the model-observation S difference, shown as color and selected model S contours, for cases (top to bottom) No DA, Surface, Glider Only, and Combined. DA analyses are used. Contours are $S = 30.5, 31.5, 32.5, 33.5$.

As seen in the observations (Figures 9a and 10a), the Columbia River plume is characterized by a layer of relatively warmer and fresher ($S < 31.5$) water near the surface. In the beginning of the series shown, before the start of the major upwelling event of 21–30 July, the glider finds the river plume waters over the shelf, close to coast. After the upwelling pushes the river plume waters offshore, the glider crosses through the river plume front on every lap between the offshore and shelf waters. Over the shelf, the glider samples through the colder and saltier upwelled waters. In particular, as seen in the data, the $S = 33.5$ isohaline is found at depths near 100 m in offshore waters and it is outcropping at the ocean surface over the shelf on 3–4 August.
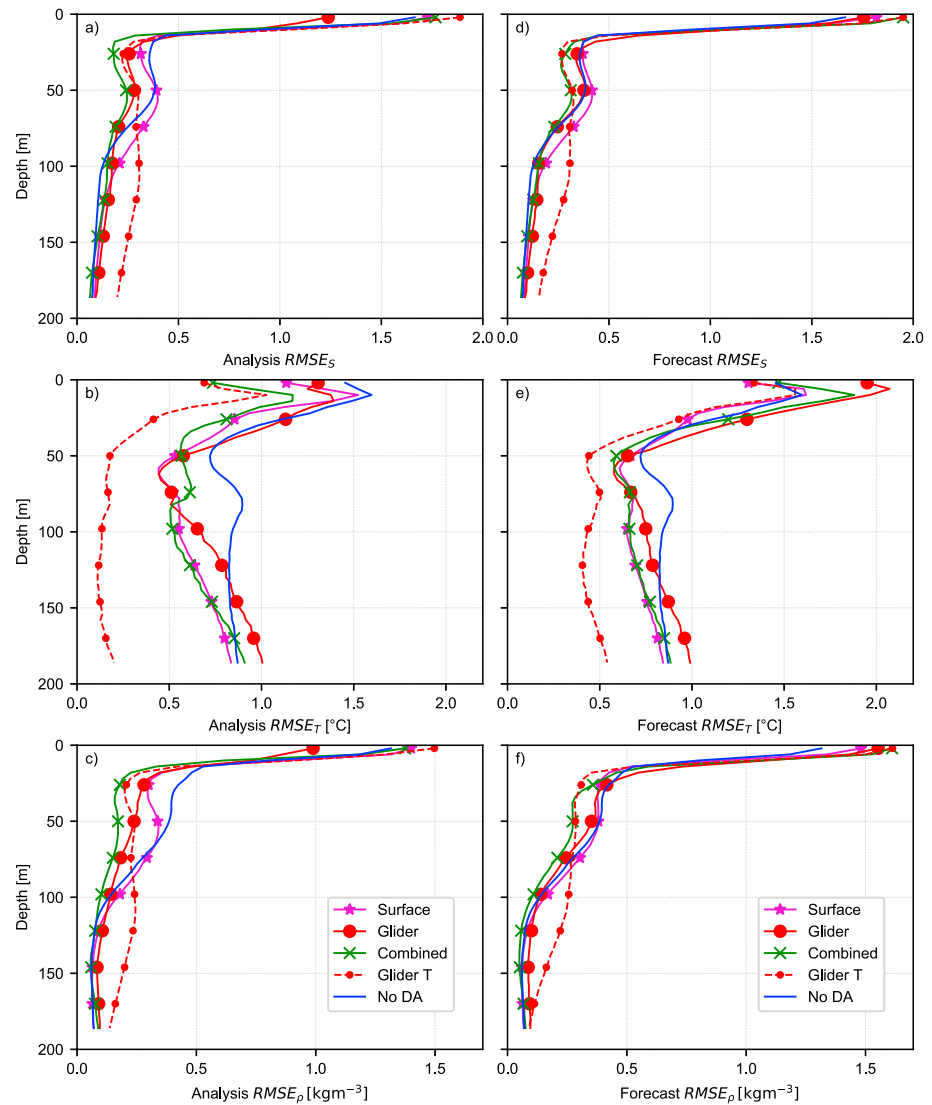
Figure 11. RMSEs from analyses (a–c) and forecasts (d–f) averaged over the period 21 July 2011 to 11 August 2011 compared to glider salinity observations (first row), glider temperature observations (second row), and potential density (third row) as functions of depth.

Every model case (Figures 9b–9e and 10b–10e) shows these patterns qualitatively correctly, although the extent of the river plume reaching the glider section line can differ from case to case. The model-data difference plot for case No DA shows the model negative bias throughout the water column in the first part of the time series (see Figure 9b). During the same time period, salinity bias is positive in the range of depths between 0 and 100 m (more precisely, between the 32.5 and 33.5 contours, Figure 10b). The DA Surface case (Figure 9c and 10c) reduces the subsurface bias in temperature between 100 m and surface. Consistent with the prescribed standard deviation in the model temperature error covariance (see section 2.5), the SST data can influence the subsurface temperature down to these depths. At the same time, the positive bias in subsurface salinity is not removed. In the latter part of the time series surface data assimilation yields increased positive temperature bias in the shallow part of the water column ($z > -50$ m). Since the DA change in salinity is not directly constrained by the salinity data and is mostly influenced by the choice of the balanced model error covariance, in which temperature correction is negatively correlated with the salinity correction, warming near the surface can be associated with a pattern of freshening the water column for $S < 33.5$ (see Figure 10c). The cases involving the glider data assimilation (i.e., Glider Only, Figures 9d and 10d, and Combined, Figures 9e and 10e) show that the DA system is able to fit both the temperature and salinity data

Table 1
RMSE for Different Types of Observations and Experiments

	Surface only	Glider only	Combined	No DA
Analysis glider S	0.27	0.21	**0.17**	0.25
Analysis glider T (°C)	0.65	0.76	**0.64**	0.84
Analysis glider ρ (kg/m^3)	0.24	0.18	**0.13**	0.27
Forecast glider S	0.29	0.25	**0.21**	0.25
Forecast glider T (°C)	**0.74**	0.83	**0.74**	0.84
Forecast glider ρ (kg/m^3)	0.27	0.25	**0.20**	0.27
Extended SST (°C)	1.09	1.77	**1.05**	1.19
Extended HFR (m/s)	**0.14**	0.27	0.16	0.17
Extended glider T (°C)	1.78	2.93	**1.20**	1.39
Extended glider S	0.61	0.62	**0.33**	0.59

Note. (top block) Depth-averaged subsurface (only including observations below 25-m depth) analysis RMSE for the period 21 July to 10 August 2011 (see Figures 11a–11c). (center block) As in top block but now for the forecast RMSE (see Figures 11d–11f). (bottom block) Forecast RMSE error over the period 8 August to 1 September (see Figure 14). In each row the case with the lowest RMSE is emphasized in bold.

and remove major biases in analyses compared to the No DA case. Qualitatively, looking at the finer details, one could favor case Combined.

Quantitative assessment is provided by calculating profiles of the model-data root-mean-square difference (or error, RMSE). These are obtained by time averaging, at each horizontal level, squares of differences as shown in Figures 9 and 10. Additionally, the RMSE for the potential density is calculated, all using the hourly model outputs. The results are presented separately for the DA analyses (Figures 11a–11c) and day 1–3 forecasts (Figure 11def). Case Surface Only produces analyses with smaller RMSE in T than case No DA throughout the water column, but with slightly larger RMSEs in S and ρ. Case Glider Only (red) yields improvement over case No DA throughout the water column in terms of T, S, and density. Case Combined has a smaller RMSE than case Glider Only in most of the water column. The notable exception is at the surface, where Case Glider Only yields the best improvement in terms of salinity (see Figure 11a) and density (see Figure 11c), but not in terms of temperature (see Figure 11b). In other words, using the surface and glider data in combination allows for a better fit to the glider data than in case Glider Only. Compared to case Surface Only case Combined shows improved fit to glider T, S, and ρ in the top 100 m of the analysis. This shows that the ratio of the observational error covariance of the glider T observations (see Figure 2) versus the observational error covariance for the SST observations ((0.39 °C)^2) is small enough that, notwithstanding that there are more SST than glider T observations, glider T observations can still contribute to the DA correction of the temperature in the vicinity of the glider transect.

For the short-term forecasts (see Figures 11d–11f), the spread between the curves is smaller than for the analyses. In particular, the improvement in T in case Combined versus case Surface Only does not persist above the 25-m depth. The result is that, at least in the vertical profiles, case Combined acts like a compromise between Glider Only and Surface Only with the glider observations providing improved forecast below the surface layer and the surface observations partially suppressing the deterioration of the forecast for the surface layer caused by the assimilation of the glider observations.

A short summary of the results from Figure 11 can be found in Table 1, which shows the time- and depth-averaged RMSE below the surface layer for analyses and forecasts over the same period. Here each row presents the estimate for a particular field (T, S, or ρ), either the analysis or the forecast. Each column corresponds to one of the base model cases. The smallest RMSE value in each row is shown as bold. Case Combined is a winner for the region below the surface layer.

A possible explanation for the fact that RMSEs for surface salinity and density are larger in case Combined compared to the analysis of case Glider Only (see Figures 11a and 11c) can lie in the structure of the background covariance error used. Figures 9b and 10b show that the plume is too fresh and too cold during the period 21–27 July. We hypothesize that DA cannot correct for the observed plume temperature and salinity
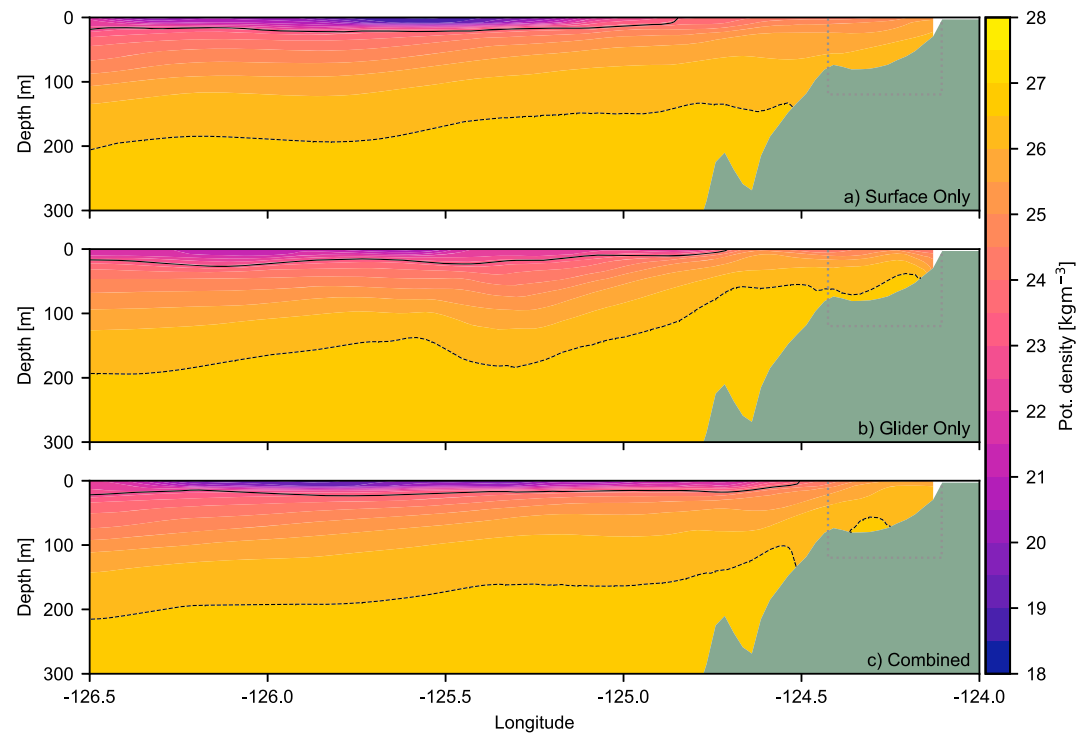
Figure 12. Daily averaged density along the line 44.64°N from the analyses on 4 August 2011 for (a) experiment Surface Only, (b) experiment Glider Only, and (c) experiment Combined. The dashed box indicates the area in which glider observations are available during this window. The dashed black line marks the 26.5-kg/m^3 isopycnal.

errors simultaneously, as in our **B** (see section 2.5) temperature and salinity background errors are assumed to have a negative correlation. In case Glider Only, DA partially reduces the salinity error at the expense of a larger temperature error, while for case Combined, in which the more numerous SST observations are present, the largest reduction of J (see (2)) is achieved by fitting the SST. To test this hypothesis, a DA experiment for the period 21 July to 11 August is performed in which glider T is only assimilated (case Glider T). The resulting RMSEs in the analysis of case Glider T show that a lower temperature RMSE can be obtained by not assimilating salinity observations (Figure 11b) and hence that it is the salinity that constrains the fit to the glider T observations. However, the reduction in T RMSE comes at the expense of an increase in glider S RMSE (Figure 11a) proving that the static **B** used is not always able to correctly represent the relationship between T and S errors in the model.

In Glider Only DA analyses, the subsurface T and S errors are reduced along the glider path. However, when we extend the cross-shore transect to the west of the glider range, problems emerge in case Glider Only. To illustrate, the potential density is calculated in a cross section at 46.64°N using daily averaged DA analysis T and S. The example of the density field on 4 August 2011 is shown in Figure 12. Also shown in the figure are the 31.5 isohaline (solid black line) and the 26.5 kg/m^3 isopycnal contour (dashed black). The former is important because it marks the edge of the Columbia River water plume. The latter is important because it marks the upper boundary of the cold, oxygen-poor, high-nutrient source water (Adams et al., 2013). Its arrival on the shelf contributes to the frequent hypoxic conditions observed on the Oregon shelf during summer (Connolly et al., 2010; Siedlecki et al., 2015). Figures 12a and 12b exhibit two noticeable differences between the cases Surface Only and Glider Only. First, glider DA affects the amount of source water (potential density >26.5 kg/m^3) predicted over the shelf. Second, west of the glider transect, at 125.3°W, the assimilation of glider data alone leaves a sizable impact on the subsurface structure. The 40-m depression of the 26.5-kg/m^3 isopycnal at 125.3°W is dynamically consistent with the erroneous anticyclonic eddy at this location in Figure 6c. Case Combined (Figure 12c) predicts denser waters over the shelf compared to case Surface Only and at the same time defies strong, possibly erroneous, corrugations of the 26.5-kg/m^3 density surface offshore of the shelf break.
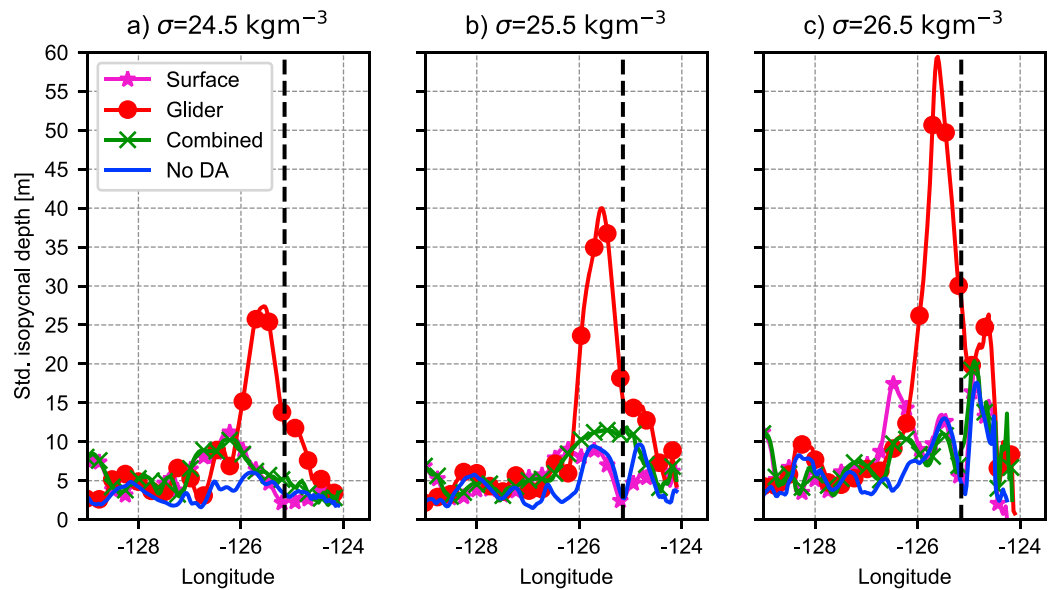
Figure 13. Standard deviation in the depths of the 24.5- (a), 25.5- (b), and 26.5-kg/m^3 (c) isopycnal from the hourly output of the analyses between 21 July and 11 August along 44.64°N, shown as functions of longitude in the different experiments. The dashed black line marks the most westward location of the glider.

To provide a more quantitative assessment of the DA impact on the depth of the subsurface isopycnal surfaces in this section, the depth of the 24.5-, 25.5-, and 26.5-kg/m^3 surfaces are calculated from the hourly snapshots over the entire period for which DA analyses are available (21 July to 11 August). The DA corrections do occasionally create an unstable profile in the surface layer in the first few hours after the correction. This makes the definition of the isopycnal depth ambiguous, in particular, for the shallower isopycnal surfaces. To overcome this problem, the model profiles are mixed into stable profiles during postprocessing before the isopycnal depth is determined (see Appendix A). For each longitude along this zonal section, the standard deviation of the hourly depths is determined (Figure 13). The standard deviation is only slightly higher for the cases Surface Only and Combined than for No DA (on average +28% and +17%, respectively, for the 26.5-kg/m^3 isopycnal surface). Five- to ten-meter deviations can be partly associated with the internal
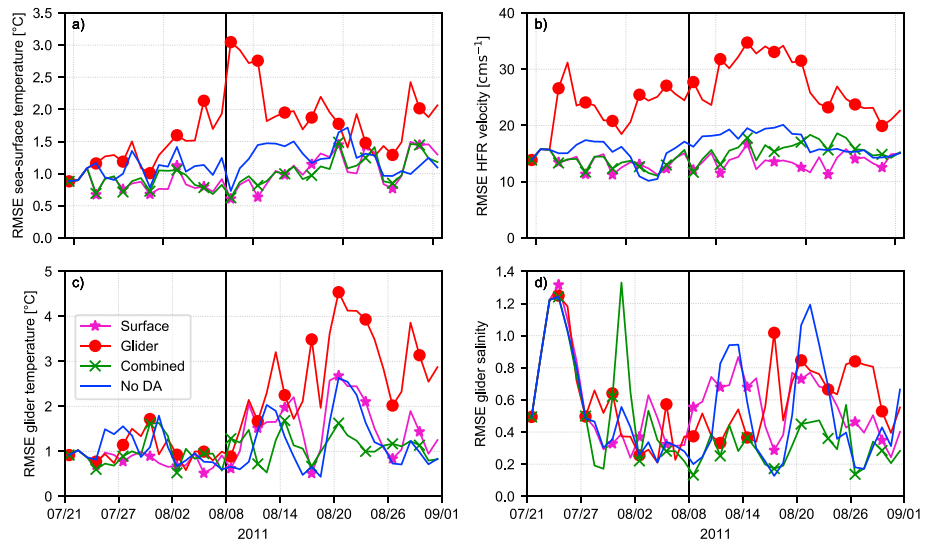
Figure 14. Times series of the area-averaged, daily averaged forecast RMSE as function of time for (a) HFR velocity, (b) SST, (c) glider temperature, and (d) glider salinity for the cases Surface Only (purple), Glider Only (red), Combined (green), and No DA (blue), respectively. The vertical lines mark the instant of the last DA correction (8 August 2011). DA = data assimilation.
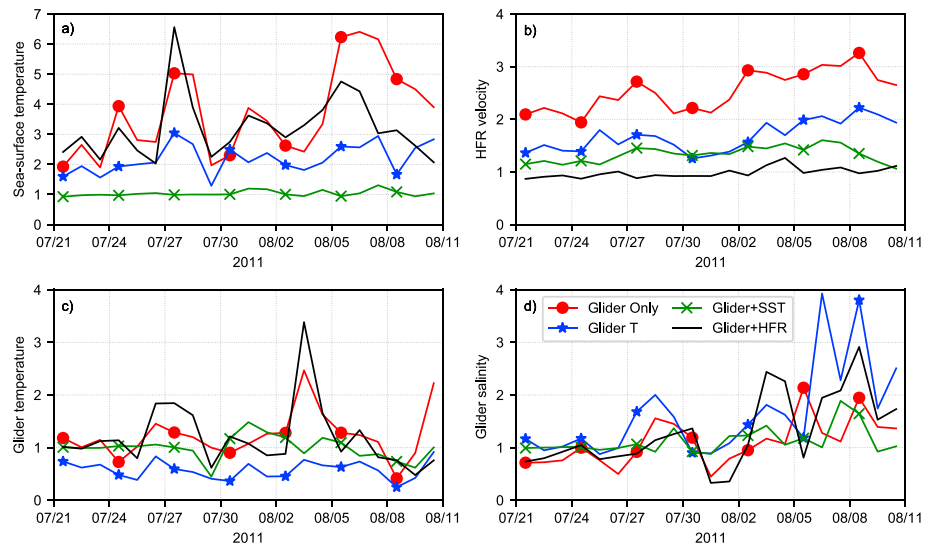
Figure 15. The time series of the daily averaged, area averaged RMSE in (a) SST, (b) HFR velocity, (c) glider temperature, (d) glider salinity observations for the DA cases, in which the subsets of the available data sets are assimilated. The values are shown relative to the RMSE for case Combined, that is, values below (above) one mean that the case is better (worse) than case Combined. Shown are DA analyses where only glider temperature and salinity (red), only glider temperature (blue), glider temperature, salinity, and SST (green), and glider temperature, salinity and HFR (black) are assimilated. RMSE = root-mean-square error; SST = sea surface temperature; HFR = high-frequency radar.

tides resolved by the 2-km model (Kurapov et al., 2003; Osborne et al., 2011). Assimilation of glider observations alone causes much greater variability along the glider transect (on average +73% increase in the standard deviation for 26.5 kg/m^3). The strongest variability is found just west of the glider transect where standard deviations can be 5–7 times as large as in the other experiments. Variability drops to levels comparable to other experiments at the distance of 80–100 km west of the glider transect, which is 3–4 times the horizontal correlation scale in the background error covariance (see section 2.5).

3.3. Post DA Persistence

After the last DA correction on 8 August, the No DA and the three DA cases are continued as forecasts until 1 September 2011. The day 1–3 forecasts (21 July to 11 August) and extended forecasts (12 August to 1 September) are compared to the HFR velocity and SST as well as glider T and S observations. The RMSE for each observation type and each day is calculated using only observations close enough to the coast and the glider section, specifically, in the shaded area in Figure 1. The area-averaged RMSE time series are presented in Figure 14. Forecast quality in the case Glider Only deteriorates quickly when compared against HFR and SST data (Figures 14a and 14b). On average over the entire period, case Combined SST RMSE is larger than the case Surface SST RMSE by only 1%; case Combined HFR RMSE is larger by only 9%. Based on these we conclude that the effect of adding the glider data on these surface fields is limited. Compared to glider T (Figure 14c), the accuracy of short-term forecasts for the Glider Only case (21 July to 8 August) is acceptable and comparable to the that from the other three cases (with RMSEs near 1 °C). However, due to DA-induced eddy transport, long-term forecasts from this case are of poor quality with RMSEs substantially higher than in the other cases as is shown in the bottom block of Table 1. The long-range forecast RMSE computed against the glider S data (Figure 14d), is large and comparable to cases No DA and Surface Only (see Table 1). The salinity RMSE for the long-range forecast following the Combined DA series of corrections is a major improvement over the other three cases. Similarly, the RMSE against glider T over this period is lower than in case Combined. These results indicate that case Combined holds an edge as both a short and longer range predictor.

3.4. Contributions From Different Observation Types

Here we answer two questions: (1) what type of the subsurface observation, T or S, is the main contributor to the deterioration of the DA results and (2) which type of surface observations provides the largest impact constraining the eddy variability over the shelf and slope. Three additional DA cases are run using subsets of the assimilation sets: Glider T, Glider+SST and Glider+HFR. In the last two cases, both glider T and S plus
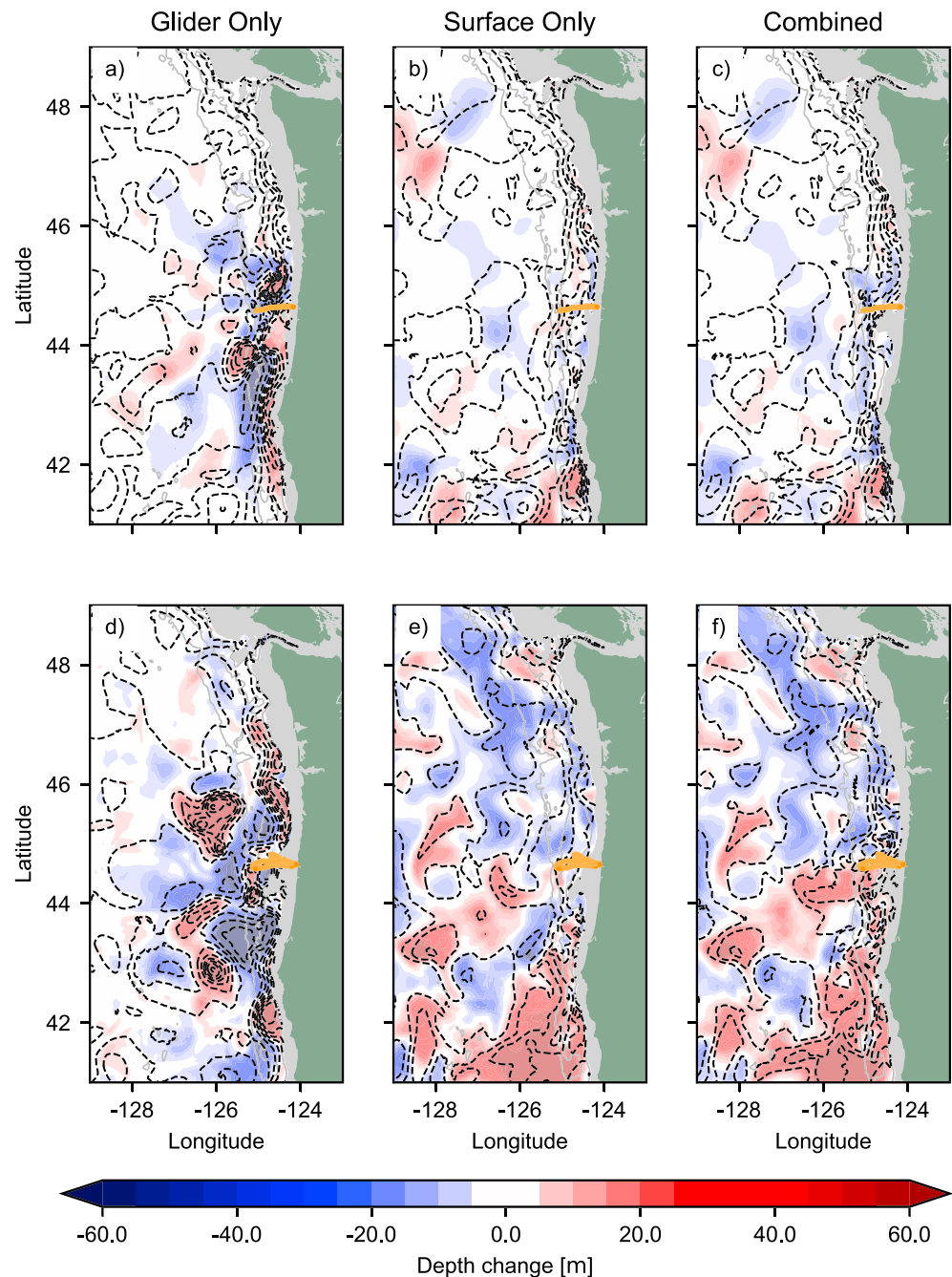
Figure 16. The $z_{26.5}$-kg/m^3 isopycnal on 21 July 2011 (a–c) and 10 August 2011 (d–f) from analysis for Glider Only (left), Surface Only (center) and Combined (right). The depth contours, every 25 m, are shown as dashed lines. The change in depth with respect to No DA is shown as color. Orange dots mark the location of the glider during up to and including the assimilation window.

one of the surface sets are assimilated. An experiment that assimilates only glider and SSH observations is not executed. as the number of SSH observations on the shelf is small and therefore it is deemed unlikely that the SSH observations are a major contributor to the improvements observed in the Combined case. The daily averaged analysis RMSEs are computed for all the cases with respect to the assimilated SST, HFR surface velocity, glider T, and S. The ratio between these RMSE and their equivalents in the case Combined is shown in Figure 15. Only observations located in the gray shelf area shown in Figure 1 are included in the calculation. The curve for the Glider Only case is added for comparison.

Figure 14c and 14d show that Case Glider T provides the best fit to glider T observations in the analysis, but at the expense of a decreasing fit to the salinity, as was already inferred from Figure 11b. Erroneous eddies are still found in case Glider T, but they are weaker than in case Glider Only and not as numerous (not shown). Consequently, Glider T provides better fit to HFR and SST observations than case Glider Only. Case Glider+SST (green line in Figure 15b) has the SST RMSE close to that in case Combined, while case Glider+HFR (black line in Figure 15b) has a velocity RMSE close to that in case Combined. These two facts suggest that corrections induced by the SST and HFR observations do not conflict with each other. SST observations contribute the most to constraining eddy variability: HFR RMSE increases only by 36% if only glider and SST are assimilated (green line in Figure 15b), while SST RSME increases by a factor of 3 in the case Glider+HFR (black line in Figure 15a). Part of this difference will stem from the fact that in case Glider+SST the number of observations assimilated is an order of magnitude larger than in Glider+HFR.

3.5. DA Impact on the Topology of the 26.5 Isopycnal Surface

Using the daily averaged temperature and salinity fields on the first day in the first data assimilation window (21 July 2011) and the last day in the last data assimilation window (10 August 2011), the depth of the 26.5-kg/m^3 isopycnal surface, $z_{26.5}$, is determined. The difference in depth of this isopycnal surface between each of the three base DA experiments and case No DA is shown in Figure 16.

In the first window, in case Glider Only (Figure 16a) the impact of the glider observations on $z_{26.5}$ is largest in the area near the glider and southward along the shelf slope where information can be propagated backward in time by the 4DVAR algorithm with coastally trapped waves (Kurapov et al., 1999, 2002, 2011). The impact in the case Combined (Figure 16b) is similar to Surface Only (Figure 16c) and differences in depth are more than a factor 2 as small as those in case Glider Only. Far away from the glider transect, corrections to $z_{26.5}$ are similar in cases Combined and Surface Only.

In the last assimilation window (Figures 16d–16f), the differences in $z_{26.5}$ between the assimilation cases and No DA are a result of the accumulated DA changes in a series of windows and their dynamical evolution over 21 days. Changes in case Glider Only reach further north and south than in Figure 16a as an assemblage of eddies. Structures in cases Surface Only and Combined are very similar. The large-scale uplifting of $z_{26.5}$ south of Cape Blanco (43°N) is associated with the correction of the location, strength, and direction of the separated coastal jet (cf. Figures 6b and 6d). The glider impact in case Combined can be seen southwest of the glider transect (44–44.6°N) where the isopycnal surface is uplifted compared to case No DA. At the beginning of our study we hypothesized that Glider Only assimilation will have a very local effect on the depth of the isopycnal surfaces and create eddies. We also hypothesized that combined assimilation of the in situ and surface data would inhibit this eddy activity. This can happen since SST (and HFR data as well) carry information about the eddy field. For example, cyclonic (anticyclonic) eddies are cold (warm) cored. If SST and HFR do not indicate an eddy at the location near the glider and if the measured stratification is significantly different from the forecast, then both the surface and subsurface data can be fit by adjusting the isopycnal surfaces at distances larger than the eddy scale. In our study we tried to demonstrate this, but could not find a clear illustration, partly since in our prior model the stratification is already close to observed (see Figure 5).

4. Conclusions and Discussion

This study shows that it can be dangerous to assimilate glider vertical profile data in a high-resolution coastal ocean model if these data are not supported by surface observations. Without the surface observations, strong eddy variability can emerge. In a high-resolution DA system, gliders will appreciate the good company of the surface data because surface maps (mostly satellite SST in our case) constrain the eddy variability and help fit both the surface and subsurface data. Combined assimilation also helps to improve the subsurface in the analyses and forecasts. However, compared to case Surface Only the improvement mainly takes place in the salinity field, while RMSEs in temperature are similar to those in Surface Only and forecast accuracy for the surface is less than in case Surface Only. The improvement in long-term subsurface forecasts can last up to 3 weeks in advance. The enstrophy (see Figure 7) can be used as a criterion for the monitoring of bogus eddy activity especially since this parameter remained very similar between cases No DA, Surface Only, and Combined, while it stood out as too large in the case Glider Only.

We find a large difference in the fit to the near-surface salinity data between the case in which unphysical eddies are formed (Glider Only) and the cases in which the erroneous eddies are not exhibited (Surface Only, Combined) or less pronounced (Glider T). This suggests that the formation of the erroneous eddy variability can in part be attributed to deficiencies in the background model T and S and a limited ability of the system to fit these data together. This can be exaggerated by the use of the static, balanced background error covariance, in which a simple negative correlation between errors in T and S is assumed, while T and S errors in the area of the river plume were sometimes positively correlated. It would be interesting to see (in future studies) if a different choice of the error covariance, for example, an ensemble-based covariance (Pasmans & Kurapov, 2017), helps to improve the fit and reduce the forecast error.

While our series of experiments concerns the glider data, we anticipate that assimilation of other in situ assets, for example, Argo profiles, can cause similar problems. We note that a useful signal in a given observed density profile can either say something about large- (basin-) scale model errors in the stratification or errors at the scale of geostrophic eddies. Li et al. (2015a, 2015b) proposed to explicitly separate the large- and small-scale signal in the observations by spatial filtering into two subsets and fit those using penalty functions with substantially different horizontal correlation scales. We had hoped that combined surface and in situ assimilation would help the system distinguish between these two scales and that DA would create subsurface corrections that reflect both the long scales and short scales. However, Figures 16b and 16c showed us that away from the glider transect corrections to the 26.5-kg/m^3 isopycnal are the same as those in case Surface Only, and hence, our study could not produce an example of large-scale subsurface corrections that can be attributed to the assimilation of glider observations.

In conclusion, the result of this study provides useful guidance for the inclusion of glider observations into the Oregon-Washington near-real-time DA system: to utilize glider observations only when SST and/or HFR coverage is good. In a near future, the SSH obtained by a wide-swath altimeter (Fu & Rodriguez, 2004) can possibly provide additional constraint limiting the erroneous eddy variability caused by in situ DA.

Appendix A: Mixing Algorithm

For a vertical column let ρ_i be the potential density in the ith layer and h_i the depth of the ith layer with $i = 1$ being the bottom layer and $i = N_z$ being the top layer. The MATLAB pseudo-code used to mix the potential density into a stable profile while preserving the depth-averaged potential density is as follows:

$$
\begin{aligned}
&\text{for } i = [N_z : -1 : 2]\\
&\quad \text{for } j = [i-1 : -1 : 1]\\
&\qquad \text{if } \rho_j < \rho_i + \delta(i-j)\\
&\qquad\quad \bar{\rho} = \left(\sum_{k=j}^{i} h_k \rho_k + \delta h_k (k-i)\right)\left(\sum_{k=j}^{i} h_k\right)^{-1}\\
&\qquad\quad \boldsymbol{\rho}_{[\mathbf{i:j}]} = \bar{\rho} + \delta(i - [j : i])\\
&\qquad \text{endif}\\
&\quad \text{endfor}\\
&\text{endfor}
\end{aligned}
$$

Here δ is the minimum density difference between two layers. For purely practical reasons δ is set to 10^{-6} kg/m^3 such that the density profile becomes a strictly monotonically decreasing function of the vertical coordinate z and can therefore be used as a vertical coordinate itself.

References

Adams, K. A., Barth, J. A., & Francis, C. (2013). Temporal variability of near-bottom dissolved oxygen during upwelling off central Oregon. *Journal of Geophysical Research: Oceans*, *118*, 4839–4854. https://doi.org/10.1002/jgrc.20361

Banas, N. S., Conway-Cranos, L., Sutherland, D. A., MacCready, P., Kiffney, P., & Plummer, M. (2015). Patterns of river influence and connectivity among subbasins of Puget Sound, with application to bacterial and nutrient loading. *Estuaries and Coasts*, *38*(3), 735–753. https://doi.org/10.1007/s12237-014-9853-y

Barth, J. A., Pierce, S. D., & Smith, R. L. (2000). A separating coastal upwelling jet at Cape Blanco, Oregon and its connection to the California Current System. *Deep Sea Research Part II: Topical Studies in Oceanography*, *47*(5), 783–810. https://doi.org/10.1016/S0967-0645(99)00127-7

Bennett, A. F. (1992). Generalized inverses of dynamical models, *Inverse Methods of the Ocean and Atmosphere* (pp. 112–150). Cambridge: Cambridge University Press.

COAPS (2015). HYCOM + NCODA global $1/12°$ analysis. Version GLBa0.08 [Database]. Retrieved from https://hycom.org/data/glba0pt08

Chapman, D. C. (1985). Numerical treatment of cross-shelf open boundaries in a barotropic coastal ocean model. *Journal of Physical Oceanography*, *15*(8), 1060–1075. https://doi.org/10.1175/1520-0485(1985)015h1060:NTOCSOi2.0.CO;2

Chelton, D. B., De Szoeke, R. A., Schlax, M. G., El Naggar, K., & Siwertz, N. (1998). Geographical variability of the first baroclinic Rossby radius of deformation. *Journal of Physical Oceanography*, *28*(3), 433–460. https://doi.org/10.1175/1520-0485(1998)028<0433:GVOTFB>2.0.CO;2

Connolly, T. P., Hickey, B. M., Geier, S. L., & Cochlan, W. P. (2010). Processes influencing seasonal hypoxia in the northern California Current System. *Journal of Geophysical Research*, *115*, C03021. https://doi.org/10.1029/2009JC005283

Courtier, P., Thépaut, J.-N., & Hollingsworth, A. (1994). A strategy for operational implementation of 4D-Var, using an incremental approach. *Quarterly Journal of the Royal Meteorological Society*, *120*(519), 1367–1387. https://doi.org/10.1002/qj.49712051912

Desroziers, G., Berre, L., Chapnik, B., & Poli, P. (2005). Diagnosis of observation, background and analysis-error statistics in observation space. *Quarterly Journal of the Royal Meteorological Society*, *131*(613), 3385–3396. https://doi.org/10.1256/qj.05.108

Dettmering, D., & Bosch, W. (2010). Global calibration of Jason-2 by multi-mission crossover analysis. *Marine Geodesy*, *33*, 150–161. https://doi.org/10.1080/01490419.2010.487779

Dobricic, S., Pinardi, N., Testor, P., & Send, U. (2010). Impact of data assimilation of glider observations in the Ionian Sea (Eastern Mediterranean). *Dynamics of Atmospheres and Oceans*, *50*(1), 78–92. https://doi.org/10.1016/j.dynatmoce.2010.01.001

Egbert, G. D., & Erofeeva, S. Y. (2002). Efficient inverse modeling of barotropic ocean tides. *Journal of Atmospheric and Oceanic Technology*, *19*(2), 183–204. https://doi.org/10.1175/1520-0426(2002)019h0183:EIMOBOi2.0.CO;2

Egbert, G. D., & Erofeeva, S. Y. (2013). TPXO7.2 atlas [Database]. Retrieved from http://volkov.oce.orst.edu/tides/global.html

Environment Canada (2015). Historical hydrometric data [Database]. Retrieved from https://wateroffice.ec.gc.ca

Erofeev, A. (2015). Gridded Slocum glider data ($1km \times 4m$) [Database]. Retrieved from https://gliderfs2.coas.oregonstate.edu/gliderweb/archive/gridded/2011/

Erofeeva, L. (2018). The Oregon Washington coastal ocean forecast system: The interactive viewer [Website]. Retrieved from http://ingria.coas.oregonstate.edu/rtdavow/index.html

Fairall, C. W., Bradley, E. F., Hare, J. E., Grachev, A. A., & Edson, J. B. (2003). Bulk parameterization of air sea fluxes: Updates and verification for the COARE algorithm. *Journal of Climate*, *16*(4), 571–591. https://doi.org/10.1175/1520-0442(2003)016<0571:BPOASF>2.0.CO;2

Flather, R. A. (1976). A tidal model of the northwest European continental shelf. *Mémoires de la Société Royale des Sciences Liège*, *10*, 141–164.

Fu, L.-L., & Rodriguez, E. (2004). High-resolution measurement of ocean surface topography by radar interferometry for oceanographic and geophysical applications. In R. S. J. Sparks & C. J. Hawkesworth (Eds.), *The State of the Planet: Frontiers and Challenges in Geophysics* (pp. 209–224). Washington, DC: American Geophysical Union.

Giddings, S. N., MacCready, P., Hickey, B. M., Banas, N. S., Davis, K. A., Siedlecki, S. A., et al. (2014). Hindcasts of potential harmful algal bloom transport pathways on the Pacific Northwest coast. *Journal of Geophysical Research: Oceans*, *119*, 2439–2461. https://doi.org/10.1002/2013JC009622

Grigori, L., Moufawad, S., & Nataf, F. (2016). Enlarged Krylov subspace conjugate gradient methods for reducing communication. *SIAM Journal of Matrix Analysis & Applications*, *37*(2), 744–773. https://doi.org/10.1137/140989492

Gürol, S., Weaver, A. T., Moore, A. M., Piacentini, A., Arango, H. G., & Gratton, S. (2014). B-preconditioned minimization algorithms for variational data assimilation with the dual formulation. *Quarterly Journal of the Royal Meteorological Society*, *140*(679), 539–556. https://doi.org/10.1002/qj.2150

Hickey, B. M., Geier, S., Kachel, N., & MacFadyen, A. (2005). A bi-directional river plume: The Columbia in summer. *Continental Shelf Research*, *25*(14), 1631–1656. https://doi.org/10.1016/j.csr.2005.04.010

Hickey, B. M., Pietrafesa, L. J., Jay, D. A., & Boicourt, W. C. (1998). The Columbia River plume study: Subtidal variability in the velocity and salinity fields. *Journal of Geophysical Research*, *103*(C5), 10,339–10,368.

Huyer, A. (1977). Seasonal variation in temperature, salinity, and density over the continental shelf off Oregon. *Limnology and Oceanography*, *22*(3), 442–453. https://doi.org/10.4319/lo.1977.22.3.0442

Huyer, A. (1983). Coastal upwelling in the California Current System. *Progress in Oceanography*, *12*(3), 259–284. https://doi.org/10.1016/0079-6611(83)90010-1

Ignatov, A., Zhou, X., Petrenko, B., Liang, X., Kihai, Y., Dash, P., et al. (2016). AVHRR GAC SST reanalysis version 1 (RAN1). *Remote Sensing*, *8*(4), 315. Data available at https://coastwatch.noaa.gov/cw_html/sst_avhrr_gac.html

Jones, E. M., Oke, P. R., Rizwi, F., & Murray, L. M. (2012). Assimilation of glider and mooring data into a coastal ocean model. *Ocean Modelling*, *47*, 1–13. https://doi.org/10.1016/j.ocemod.2011.12.009

Koch, A. O., Kurapov, A. L., & Allen, J. S. (2010). Near-surface dynamics of a separated jet in the coastal transition zone off Oregon. *Journal of Geophysical Research*, *115*, C08020. https://doi.org/10.1029/2009JC005704

Kosro, P. M. (2005). On the spatial structure of coastal circulation off Newport, Oregon, during spring and summer 2001 in a region of varying shelf width. *Journal of Geophysical Research*, *110*, C10S06. https://doi.org/10.1029/2004JC002769

Kosro, P. M. (2017). HFRnet: HF radar national network production TDS. Retrieved from http://hfrnet-tds.ucsd.edu/thredds/HFRADAR_USWC_hourly_RTV.html

Kurapov, A. L., Allen, J. S., Miller, R. N., & Egbert, G. D. (1999). Generalized inverse for baroclinic coastal flows. In *Proceedings of the 3rd Conference on Coastal Atmospheric and Oceanic Prediction and Processes*, pp. 3–5.

Kurapov, A. L., Egbert, G. D., Allen, J. S., & Miller, R. N. (2009). Representer-based analyses in the coastal upwelling system. *Dynamics of Atmospheres and Oceans*, *48*(13), 198–218. https://doi.org/10.1016/j.dynatmoce.2008.09.002

Kurapov, A. L., Egbert, G. D., Allen, J. S., Miller, R. N., Erofeeva, S. Y., & Kosro, P. M. (2003). The M2 internal tide off Oregon: Inferences from data assimilation. *Journal of Physical Oceanography*, *33*(8), 1733–1757. https://doi.org/10.1175/1520-0485(2003)033<1733:TMITOO>2.0.CO;2

Kurapov, A. L., Egbert, G. D., Miller, R. N., & Allen, J. S. (2002). Data assimilation in a baroclinic coastal ocean model: Ensemble statistics and comparison of methods. *Monthly Weather Review*, *130*(4), 1009–1025. https://doi.org/10.1175/1520-0493(2002)130<1009:DAIABC>2.0.CO;2

Kurapov, A. L., Foley, D., Strub, P. T., Egbert, G. D., & Allen, J. S. (2011). Variational assimilation of satellite observations in a coastal ocean model off Oregon. *Journal of Geophysical Research*, *116*, C05006. https://doi.org/10.1029/2010JC006909

Kurapov, A. L., & Pasmans, I. (2018). AVRORA 4DVAR: Balance operator-glider experiment (Version 1.0.0) [Software repository]. https://doi.org/10.5281/zenodo.1256195

Labroue, S., Boy, F., Picot, N., Urvoy, M., & Ablain, M. (2012). First quality assessment of the Cryosat-2 altimetric system over ocean. *Advances in Space Research*, *50*(8), 1030–1045. https://doi.org/10.1016/j.asr.2011.11.018

Li, Z., Chao, Y., Farrara, J. D., & McWilliams, J. C. (2013). Impacts of distinct observations during the 2009 Prince William Sound field experiment: A data assimilation study. *Continental Shelf Research*, *63*, S209–S222. https://doi.org/10.1016/j.csr.2012.06.018

Li, Z., McWilliams, J. C., Ide, K., & Farrara, J. D. (2015a). A multiscale variational data assimilation scheme: Formulation and illustration. *Monthly Weather Review*, *143*(9), 3804–3822. https://doi.org/10.1175/MWR-D-14-00384.1

Li, Z., McWilliams, J. C., Ide, K., & Farrara, J. D. (2015b). Coastal ocean data assimilation using a multi-scale three-dimensional variational scheme. *Ocean Dynamics*, *65*(7), 1001–1015. https://doi.org/10.1007/s10236-015-0850-x

Liu, Y., MacCready, P., & Hickey, B. M. (2009). Columbia River plume patterns in summer 2004 as revealed by a hindcast coastal ocean circulation model. *Geophysical Research Letters*, *36*, L02601. https://doi.org/10.1029/2008GL036447

MacCready, P., & Giddings, S. N. (2016). The mechanical energy budget of a regional ocean model. *Journal of Physical Oceanography*, *46*(9), 2719–2733. https://doi.org/10.1175/JPO-D-16-0086.1

Marchesiello, P., McWilliams, J. C., & Shchepetkin, A. (2001). Open boundary conditions for long-term integration of regional oceanic models. *Ocean Modelling*, *3*(1), 1–20. https://doi.org/10.1016/S1463-5003(00)00013-5

Matthews, D., Powell, B. S., & Janeković, I. (2012). Analysis of four-dimensional variational state estimation of the Hawaiian waters. *Journal of Geophysical Research*, *117*, C03013. https://doi.org/10.1029/2011JC007575

Mazzini, P. L. F., Barth, J. A., Shearman, R. K., & Erofeev, A. (2014). Buoyancy-driven coastal currents off Oregon during fall and winter. *Journal of Physical Oceanography*, *44*(11), 2854–2876. https://doi.org/10.1175/JPO-D-14-0012.1

Melet, A., Verron, J., & Brankart, J.-M. (2012). Potential outcomes of glider data assimilation in the Solomon Sea: Control of the water mass properties and parameter estimation. *Journal of Marine Systems*, *94*, 232–246. https://doi.org/10.1016/j.jmarsys.2011.12.003

Mellor, G. L., & Yamada, T. (1982). Development of a turbulence closure model for geophysical fluid problems. *Reviews of Geophysics*, *20*(4), 851–875. https://doi.org/10.1029/RG020i004p00851

Mooers, C. N. K., Collins, C. A., & Smith, R. L. (1976). The dynamic structure of the frontal zone in the coastal upwelling region off Oregon. *Journal of Physical Oceanography*, *6*(1), 3–21. https://doi.org/10.1175/1520-0485(1976)006<0003:TDSOTF>2.0.CO;2

NANOOS (2018). NVS: Data explorer [Website]. Retrieved from http://nvs.nanoos.org/Explorer

National Centers for Environmental Prediction, NCEP (2015a). U.S. coastal relief model (CRM). Vol. 7 and 8 [Database]. Retrieved from https://www.ngdc.noaa.gov/mgg/coastal/crm.html

NCEP (2015b). 2-minute gridded global relief data (ETOPO2v2) [Database]. https://doi.org/10.7289/V5J1012Q

NCEP (2015c). NCEP North American Mesoscale (NAM) 12 km analysis [Database]. Retrieved from https://www.ncei.noaa.gov/thredds/catalog/namanl/catalog.html

NDBC (2016). National Data Buoy Center [Database]. Retrieved from http://www.ndbc.noaa.gov/

Ngodock, H., & Carrier, M. (2014). A 4DVAR system for the Navy Coastal Ocean Model. Part II: Strong and weak constraint assimilation experiments with real observations in Monterey Bay. *Monthly Weather Review*, *142*(6), 2108–2117. https://doi.org/10.1175/MWR-D-13-00220.1

Ocean Observatories Initiative (2018). Mobile assets (CE05MOAS) [Website]. Retrieved from http://oceanobservatories.org/site/ce05moas/

Oke, P. R., Allen, J. S., Miller, R. N., & Egbert, G. D. (2002). A modeling study of the three-dimensional continental shelf circulation off Oregon. Part II: Dynamical analysis. *Journal of Physical Oceanography*, *32*(5), 1383–1403. https://doi.org/10.1175/1520-0485(2002)032<1383:AMSOTT>2.0.CO;2

Oke, P. R., Allen, J. S., Miller, R. N., Egbert, G. D., Austin, J. A., Barth, J. A., et al. (2002). A modeling study of the three-dimensional continental shelf circulation off Oregon. Part I: Model-data comparisons. *Journal of Physical Oceanography*, *32*(5), 1360–1382. https://doi.org/10.1175/1520-0485(2002)032<1360:AMSOTT>2.0.CO;2

Oke, P. R., Allen, J. S., Miller, R. N., Egbert, G. D., & Kosro, P. M. (2002). Assimilation of surface velocity data into a primitive equation coastal ocean model. *Journal of Geophysical Research*, *107*(C9), 3122. https://doi.org/10.1029/2000JC000511

Osborne, J. J., Kurapov, A. L., Egbert, G. D., & Kosro, P. M. (2011). Spatial and temporal variability of the M2 internal tide generation and propagation on the Oregon shelf. *Journal of Physical Oceanography*, *41*(11), 2037–2062. https://doi.org/10.1175/JPO-D-11-02.1

Pan, C., Zheng, L., Weisberg, R. H., Liu, Y., & Lembke, C. E. (2014). Comparisons of different ensemble schemes for glider data assimilation on West Florida Shelf. *Ocean Modelling*, *81*, 13–24. https://doi.org/10.1016/j.ocemod.2014.06.005

Pasmans, I. (2018). Why gliders appreciate good company: Postprocessing files (Version 1.1.1) [Software repository]. https://doi.org/10.5281/zenodo.1419351

Pasmans, I., & Kurapov, A. L. (2017). A Monte Carlo background covariance localization method for an ensemble variational assimilation system. *Monthly Weather Review*, *145*(11), 4543–4557. https://doi.org/10.1175/MWR-D-16-0424.1

Pasmans, I., & Kurapov, A. L. (2018). Why gliders appreciate good company: Experimental set-up [Software repository]. https://doi.org/10.5281/zenodo.1206303

Pawlowicz, R., Beardsley, B., & Lentz, S. (2002). Classical tidal harmonic analysis including error estimates in MATLAB using T_Tide. *Computers & Geosciences*, *28*(8), 929–937. https://doi.org/10.1016/S0098-3004(02)00013-4

Saldías, G. S., Shearman, R. K., Barth, J. A., & Tufillaro, N. (2016). Optics of the offshore Columbia River plume from glider observations and satellite imagery. *Journal of Geophysical Research: Oceans*, *121*, 2367–2384. https://doi.org/10.1002/2015JC011431

Scharroo, R., Leuliette, E. W., Lillibridge, J. L., Byrne, D., Naeije, M. C., & Mitchum, G. T. (2013). RADS: Consistent multi-mission products, *20*. (Vol. 20, p. 4). ESA SP-710. (Data available at http://rads.tudelft.nl/rads/rads.shtml).

Shchepetkin, A. F., & McWilliams, J. C. (2003). A method for computing horizontal pressure-gradient force in an oceanic model with a nonaligned vertical coordinate. *Journal of Geophysical Research*, *108*(C3), 3090. https://doi.org/10.1029/2001JC001047

Shchepetkin, A. F., & McWilliams, J. C. (2005). The Regional Oceanic Modeling System (ROMS): A split-explicit, free-surface, topography-following-coordinate oceanic model. *Ocean Modelling*, *9*(4), 347–404. https://doi.org/10.1016/j.ocemod.2004.08.002

Shulman, I., Rowley, C., Anderson, S., DeRada, S., Kindle, J., Martin, P., et al. (2009). Impact of glider data assimilation on the Monterey Bay model. *Deep Sea Research Part II: Topical Studies in Oceanography*, *56*(35), 188–198. https://doi.org/10.1016/j.dsr2.2008.08.003

Siedlecki, S. A., Banas, N. S., Davis, K. A., Giddings, S., Hickey, B. M., MacCready, P., et al. (2015). Seasonal and inter-annual oxygen variability on the Washington and Oregon continental shelves. *Journal of Geophysical Research: Oceans*, *120*, 608–633. https://doi.org/10.1002/2014JC010254

Sikirić, M. D., Janeković, I., & Kuzmić, M. (2009). A new approach to bathymetry smoothing in sigma-coordinate ocean models. *Ocean Modelling*, *29*(2), 128–136. https://doi.org/10.1016/j.ocemod.2009.03.009

Towns, J., Cockerill, T., Dahan, M., Foster, I., Gaither, K., Grimshaw, A., et al. (2014). XSEDE: Accelerating scientific discovery. *Computing in Science & Engineering*, *16*(5), 62–74. https://doi.org/10.1109/MCSE.2014.80

USGS (2015). National Water Information System [Database]. Retrieved from https://waterdata.usgs.gov/usa/nwis/

Weaver, A. T., Deltel, C., Machu, E., Ricci, S., & Daget, N. (2005). A multivariate balance operator for variational ocean data assimilation. *Quarterly Journal of the Royal Meteorological Society*, *131*(613), 3605–3625. https://doi.org/10.1256/qj.05.119

Yu, P., Kurapov, A. L., Egbert, G. D., Allen, J. S., & Kosro, P. M. (2012). Variational assimilation of HF radar surface currents in a coastal ocean model off Oregon. *Ocean Modelling*, *49-50*, 86–104. https://doi.org/10.1016/j.ocemod.2012.03.001

Zhang, W. G., Wilkin, J. L., & Arango, H. G. (2010). Towards an integrated observation and modeling system in the New York Bight using variational methods. Part I: 4DVAR data assimilation. *Ocean Modelling*, *35*(3), 119–133. https://doi.org/10.1016/j.ocemod.2010.08.003